

\*\*\*\*\*  
*This manuscript has been submitted for publication in TECTONOPHYSICS. Please note that it has yet to be formally accepted for publication. Subsequent versions of this manuscript may have slightly different content. If accepted, the final version of this manuscript will be available via the 'Peer-reviewed Publication DOI' link on the right-hand side of this webpage.*  
\*\*\*\*\*

# **Protracted thermal evolution of the Neoproterozoic Araçuaí hot orogen (SE Brazil): consequences for rheology, strain distribution, and deformation analysis**

Alain Vauchez<sup>1\*</sup>, Maria Helena B.M. Hollanda<sup>2</sup>, Patrick Monié<sup>1</sup>, Mathieu Mondou<sup>1,2</sup>, Marcos Egydio-Silva<sup>2</sup>

<sup>(1)</sup> Géosciences Montpellier, Université de Montpellier & CNRS, Place E. Bataillon, 34095 Montpellier Cedex 05, France

<sup>(2)</sup> Instituto de Geociências, Universidade de São Paulo, Rua do Lago, 562, 05508-080 São Paulo, Brazil

## ***Abstract:***

The Araçuaí-Ribeira belt formed during the amalgamation of West Gondwana in the late Neoproterozoic. Its evolution encompasses a main tectono-metamorphic peak at 600-580 Ma and a minor one, associated with the final collision with the Western Congo at 540-530 Ma. This belt holds characteristics of a hot-orogen: high thermal gradient ( $>30$  °C/km), pervasive partial melting of the middle crust, emplacement of huge volume of magmas resulting from partial melting of the lower crust and underlying mantle, and slow cooling after the peak of temperature. We report 21 new amphibole, biotite and muscovite  $^{40}\text{Ar}/^{39}\text{Ar}$  ages, which complement data already published by our group. Altogether, these data support slow cooling (3-4 °C/Myr) during several tens of million years after the peak temperature ( $\sim 800$  °C at  $\sim 600$  Ma), followed by faster cooling ( $>10$  °C/Myr) after the final amalgamation of Western Gondwana. We estimate that  $\sim 30$  Myr were needed to heat the middle crust to the peak of temperature and that anatectic and plutonic bodies remained in the magmatic state over at least 40 Myr. This protracted thermal evolution likely had major effects on the rheology of the middle crust and on the tectonic evolution of this orogen. For instance, correlation of U-Pb zircon crystallization ages and  $^{40}\text{Ar}/^{39}\text{Ar}$  biotite cooling ages in the anatectic core of the orogen denotes a diachronic thermal evolution likely related to a 3D deformation characterized by successive upwelling of anatectic components, along a channel crosscutting pre-existent fabric (channel-flow type). This study also highlights that classical structural analysis techniques relying on changes in pressure or temperature conditions to identify the succession of deformation phases, cannot be used to decipher the tectonic evolution of hot, slowly cooling orogenic belts, where temperature varies weakly over tens of millions of years, allowing diachronic episodes of deformation to occur under almost similar pressure and temperature conditions.

\* Corresponding author - email address: alain.vauchez@umontpellier.fr



Keywords: Hot orogen,  $^{40}\text{Ar}/^{39}\text{Ar}$  ages, slow cooling, crust rheology, gravity-induced 3D deformation.

- 1) Slow cooling of the Neoproterozoic Araçuaí hot orogen
- 2) Middle crust partially molten during 40-45 Ma
- 3) Rheology of the crust and strain distribution
- 4) Thermo-tectonic evolution

## **1. Introduction:**

Many orogens are characterized by an abnormally high geotherm ( $\geq 30$  °C/km) down to the middle/lower crust (e.g., Peucat et al., 1999; Möller et al., 2000; Collins, 2002; Morisset et al., 2009; Högdahl et al., 2012; Turlin et al., 2018). A common characteristic of these "large-hot" orogens (Beaumont et al., 2010) is to have cooled very slowly; estimated cooling rates are usually  $\ll 10$  °C/Myr. Thus, after temperature rose up to the metamorphic peak, it remained high over millions of years. The effects of this peculiar thermal evolution on the mechanical behavior of the lithosphere and on petrologic and geochemical systems are still not fully evaluated (e.g., Jamieson et al., 2011). Such an evolution contrasts with those of "small-cold", "alpine-type" orogens (Beaumont et al., 2010), in which temperature variations during and following orogeny are much faster. Cooling rates are in most cases high (several tens of °C/Myr) and, sometimes, even higher, in particular when fast exhumation follows orogen building (e.g., Zeck et al., 1992; Janots et al., 2009). Rapid temperature variations result in marked changes in the rheology of rocks over short periods of time and successive stages of the orogenic evolution are usually recorded as superimposed deformations occurring at different pressure and temperature conditions. In contrast, in a hot-orogen, temperature decreases very slowly; diachronic deformation episodes may occur under similar temperature conditions and, hence, result in similar rock microstructures and mineralogical assemblages. Consequently, it might be difficult to recognize contemporaneous deformations with contrasted kinematics from diachronous deformations separated by 10-15 Myr, for instance.

The processes that result in the formation of "hot orogens" are still poorly understood. Radiogenic heating of a highly thickened continental crust is regarded as the most efficient one (England and Thompson, 1986; Huerta et al., 1998; Vanderhaeghe et al., 2003; Clark et al., 2011; Clark et al., 2015). However, mechanical heating due to shearing or intrusion of multiple batches of mantle-derived magmas may also contribute to generate abnormally high temperatures in the middle to lower crust (Michaut and Jaupart, 2007; Nabelek et al., 2010).

At larger scales, it was suggested that slab-retreat might trigger upwelling of asthenospheric mantle, which may contribute to heating of the overlying plate (e.g., Turlin et al., 2018 and references therein).

Three processes may combine to lower the cooling rates in a collision zone:

- High temperature in the middle crust decreases its thermal conductivity and hence its capacity to evacuate heat. A "heat reservoir" may thus form in the middle/lower crust, allowing for maintenance of an abnormal thermal gradient over long periods of time (Michaut and Jaupart, 2007; Whittington et al., 2009; Nabelek et al., 2010).

- High temperature in the middle to lower crust may trigger widespread partial melting and emplacement of large volumes of magma in the middle crust. Upon cooling, crystallization of these magmas releases latent heat of crystallization that compensates, at least partially, conductive cooling (Michaut and Jaupart, 2011).

- The viscosity of a hot and partially molten middle crust is too low to sustain high topography. When the weight due to orogenic topography exceeds the strength of the hot middle crust, it triggers a gravity-driven flow in the low-viscosity middle to lower crust, which reduces the topography and forms plateaus (e.g., Jamieson et al., 2011 and references therein). This process partly compensates orogenic thickening of the crust through frontal or/and lateral extrusion, limits erosion rates, and, consequently, hinders tectonic exhumation and associated cooling.

In Southeast Brazil, the Araçuaí belt (Figure 1) displays evidence of high temperature contractional deformation distributed almost homogeneously all over its internal domain on which focus this study, which is ~200 km large and >500 km long. Pressure-temperature estimates consistently point to synkinematic conditions between ~750 °C/500-600 MPa and ≥800 °C/600-700 MPa (Petitgirard et al., 2009; Cavalcante et al., 2014; Moraes et al., 2015; Richter et al., 2016), supporting a temperature gradient of 30-35 °C/km down to 25 km depth at least. Cavalcante et al. (2018) have also substantiated that anatexis was active in the core of the belt during ~30 Myr. However, cooling rates were poorly constrained. Only two amphibole and three biotite <sup>40</sup>Ar/<sup>39</sup>Ar ages from four samples, suggesting low cooling rate, have been previously published (Petitgirard et al., 2009). Here, we report 21 new <sup>40</sup>Ar/<sup>39</sup>Ar ages in amphibole, muscovite and biotite from 16 samples representative of the different tectonic units of the Araçuaí "hot orogen". These new data, combined with previously published U-Pb zircon ages, thermo-barometric data, and structural data from field measurements and Anisotropy of Magnetic Susceptibility (AMS) mapping (Vauchez et al., 2007; Petitgirard et al., 2009; Mondou et al., 2012; Cavalcante et al., 2013, 2014, 2018)

constrain a protracted tectono-thermal evolution for this orogenic belt and confirm that temperatures in the middle crust remained high over tens of Myr. Based on these results, we discuss the implications of such an evolution for the strain repartition through space and time in this orogenic segment and the difficulties in applying classical tectonic analysis to hot orogens.

## **2. *Structure of the Araçuaí belt and previous thermo-chronological data***

The Araçuaí belt (Figure 1) is a segment of a large orogenic system formed between the São Francisco, Salvador, and Congo cratons during the convergence between the South America and Africa proto-continents, which resulted in the formation of Western Gondwana (Hasui et al., 1975; Almeida, 1977; Trompette et al., 1992; Pedrosa-Soares et al., 2007). The bulk orogenic system comprises the Araçuaí-Ribeira and Cabo Frio-West Congo belts (Monié et al., 2012; Egydio-Silva et al., 2018). The convergence lasted at least one hundred millions years and diachronic orogenic climaxes have been substantiated for the Araçuaí-Ribeira orogen (600-570 Ma; e.g., Nalini et al., 2000b; Mondou et al., 2012; Gonçalves et al., 2014; Cavalcante et al., 2018) and for the West Congo belt (540-530 Ma; e.g., Monié et al. 2012). The latter event involved thrusting of the "Cabo Frio Tectonic Domain" upon the eastern Ribeira belt in the Rio de Janeiro province (Schmitt et al., 2004).

On the South American side, the Araçuaí-Ribeira belt molds the eastern to southeastern boundary of the São Francisco craton (Vauchez et al., 1994; Egydio-Silva et al., 2018; Figure 1). The Ribeira belt forms the southern segment of the orogen. It is characterized by a transpressional tectonic regime, which combined orogen-parallel transcurrent motion with orogen-normal thrusting (Vauchez et al., 1994; Egydio-Silva et al., 2002). Seismic anisotropy measurements (Heintz et al., 2003; Assumpção et al., 2006) suggest that orogen-parallel shearing involved the whole lithosphere (Vauchez et al., 2012). Northward, the connection with the Araçuaí belt is characterized by a curvature of the orogenic fabric from NE-SW to N-S (Figure 1) and a progressive transition in strain regime to dominant westward thrusting of allochthonous units onto the São-Francisco craton in the Araçuaí belt (Vauchez et al., 1994; Oliveira et al., 2000; Egydio-Silva et al., 2005; Vauchez et al., 2007; Egydio-Silva et al., 2018). These longitudinal variations in orogenic fabric and kinematics are likely related to the termination of the São Francisco craton (Vauchez et al. 1994). Finally, the northern termination of the Araçuaí belt is characterized by dominant northward thrusting of the orogenic units onto the Salvador craton (e.g., Uhlein et al., 1998).

The central Araçuaí belt (Figure 2), where all samples used in this study were collected (location of selected samples in Supplementary Material #1), is composed by four allochthonous domains docked against the São Francisco craton (Oliveira et al., 2000; Vauchez et al., 2007). These domains are from West to East:

- The *para-autochthonous metasedimentary cover* of the craton. Several U-Pb and  $^{207}\text{Pb}/^{206}\text{Pb}$  ages in zircons > 2 Ga obtained in this domain (e.g., Noce et al., 2000; Silva et al., 2002) support that these rocks belong to the craton. Approaching the contact with the allochthonous units, these rocks display a tectonic fabric parallel to the mylonitic fabric of the westernmost allochthonous unit, suggesting that they have been both strongly deformed under high temperature conditions during the Neoproterozoic orogeny. The foliation gently dips eastward and the lineation trends dominantly EW (Figure 2), metapelites contain acicular sillimanite, garnet, and K-feldspar and coarse-grained quartzites contain crystals of sillimanite frequently included in overgrown quartz grains. Shear criteria, although infrequent, consistently point to a top-to-west sense of shear.

- The *Western Mylonitic Unit (WMU)* (Figure 2) is thrust westward onto the para-autochthonous cover of the craton. This unit comprises mylonites derived from metasediments, which display a foliation that gently dips eastward and bears an EW-trending lineation formed under HT-LP conditions (Petitgirard et al., 2009). The similarity of lithologies and deformation conditions with those of the para-autochthonous cratonic formations hinders a precise definition of the basal contact of the WMU. The main differences between the two units are the presence in the WMU of numerous top-to-west shear criteria (Figure 3a-d), the absence of quartzites, the alternation of metapelites with amphibolites, and the presence of large volumes (up to 40% locally) of anatectic leucogranites in decimetric veins parallel to the mylonitic foliation (Figure 3b-d). There is no evidence of strain localization at the base of the unit; strain is rather homogeneously distributed across the WMU. Indeed, the microstructure of the HT mylonites is similar across the whole unit, varying only as a function of mineralogy. Petitgirard et al. (2009) have determined metamorphic conditions for the WMU mylonites based on garnet-biotite exchange thermobarometers: core-core analyses (or biotite included in garnet) consistently yield 760-780°C ( $\pm 30^\circ\text{C}$ ) and rim-rim analyses, 730-760°C ( $\pm 30^\circ\text{C}$ ) and pressure in the range 500-600 MPa. A few ages have been published for this unit. Using the Pb-evaporation technique Noce et al. (2000) have dated two magmatic bodies (Brasilândia and Guarataia plutons) from this unit (Oliveira et al., 2000), which yielded  $^{207}\text{Pb}/^{206}\text{Pb}$  zircon ages of  $595 \pm 3$

and  $574 \pm 2$  Ma respectively, later on confirmed by Tadeschi et al. (2016). Petitgirard et al. (2009) have dated two synkinematic leucocratic granites intercalated in the mylonites: one yielded U-Pb ages of  $577 \pm 9$  Ma for zircon and  $572 \pm 3$  Ma for monazite and the other yielded a zircon U-Pb age of  $578 \pm 3$  Ma (Figure 4; Table 1). These authors have reported  $^{40}\text{Ar}/^{39}\text{Ar}$  ages of ca. 501 and ca. 495 Ma for amphiboles and ca. 474 and ca. 468 Ma for biotites from the WMU and the associated Ibituruna syenite, respectively; these preliminary data are integrated in our database (Table 1, Figure 7) and further commented (see Supplementary Material #2 for amphibole AR-414 from the Ibituruna syenite).

- The *Central Plutonic Unit* (CPU; Figure 2) comprises huge volumes of synkinematic garnet-bearing granodiorites and tonalites emplaced in metasediments (e.g., Mondou et al., 2012; Narduzzi et al., 2017). These plutonic bodies (the "São Vitor" and "Galileia" batholiths) display a consistent magmatic fabric (Figure 5) that evolves eastwards from a gently eastward-dipping foliation bearing a dominantly EW-trending lineation to a steeply-dipping to subvertical foliation bearing a lineation that switches from subvertical to subhorizontal over intervals of a few tens of meters. In the easternmost part of the CPU, Mondou et al. (2012) have substantiated the presence of a corridor in which the magmatic foliation is subhorizontal and bears a strong orogen-parallel, NS-trending magmatic lineation. In several places, the granodiorites and tonalites contain elongated dioritic to gabbroic lenses (Vauchez et al., 2007; Gonçalves et al., 2014; Narduzzi et al., 2017) implying in a contribution of mantle-derived magmas to the formation of the batholiths (Figure 5c).

Metamorphic conditions in the metasedimentary country rocks of the CPU are still poorly constrained due to poor outcropping conditions, but they tend to decrease eastwards as supported by the occurrence of staurolite and, locally, of muscovite in garnet-sillimanite bearing metapelites of the easternmost part of the CPU. These minerals, indicative of temperatures  $\leq 650$  °C (Nalini et al., 2015), are only present in the easternmost CPU.

Several ages have been obtained for CPU granitoids close to the contact with the WMU (Figure 4). Zircons from a tonalite sill yielded a U-Pb age of  $580 \pm 8$  Ma (Petitgirard et al., 2009). Two leucocratic veins interlayered with mylonitic metasediments yielded zircon U-Pb ages of  $587 \pm 5$  and  $579 \pm 8$  Ma (Mondou et al., 2012). Zircons from a sample of tonalite collected ~80 km south of the previous locations and ascribed to the CPU western boundary yielded an age of  $597 \pm 4$  Ma (Gonçalves et al., 2014).

The São Vitor tonalite was first dated at  $576 \pm 5$  and  $569 \pm 9$  Ma (Noce et al., 2000;  $^{207}\text{Pb}/^{206}\text{Pb}$  ages on zircons) then, Mondou et al. (2012) obtained one U-Pb and two  $^{207}\text{Pb}/^{206}\text{Pb}$  ages on zircons of  $583 \pm 4$ ,  $583 \pm 4$ ,  $582 \pm 6$ , and  $585 \pm 4$  Ma, respectively.

The Galileia tonalitic/granodioritic batholith was dated at  $594 \pm 6$  Ma (Nalini et al., 2000b;  $^{206}\text{Pb}/^{238}\text{U}$  on zircons). Subsequently, Mondou et al. (2012) have dated samples from domains of this batholith presenting contrasted fabrics. U-Pb zircon ages from these domains with different kinematics are fairly consistent between 579 and 583 Ma.

The muscovite-bearing Palmital peraluminous granite was dated at  $582 \pm 2$  Ma (Nalini et al., 2000a) and the cordierite-garnet-biotite-bearing Wolf leucogranite at  $582 \pm 5$  Ma (Noce et al., 2000) and  $585 \pm 4$  Ma (U-Pb on zircons; Mondou et al., 2012). These two granites (Figures 2, 4) likely result from melting of aluminous metapelites contemporaneous to the melting of the lower crust and underlying mantle that formed the tonalitic/granodioritic magmas.

- *Intermediate, discontinuous kinzigitic unit* (Figures 2 and 6). The steeply dipping, medium temperature, staurolite-bearing metasediments that crop out in the easternmost part of the CPU are separated from the gently dipping Eastern Anatectic Unit (EAU; see below) by a discontinuous unit of partially molten kinzigites with a steeply-dipping foliation (Oliveira et al., 2000; Mondou et al., 2012). In contrast with metasediments of the easternmost CPU, these kinzigites contain biotite, garnet, cordierite, sillimanite, but no staurolite or muscovite. The tectonic contact between these kinzigites and the CPU is therefore characterized by a metamorphic gap, despite the similar subvertical fabric recorded by the two units. This suggests that the intermediate kinzigitic unit, initially equilibrated at deeper levels, has been thrust upon the CPU and that, subsequently, the tectonic contact and associated fabric have been verticalized.

- The *Eastern Anatectic Unit* (EAU, also known as "*Carlos Chagas leucogranite*"; Figures 2 and 6) is more than 300 km long and 50 to 100 km wide. It comprises peraluminous metatexites, diatexites, and leucogranites containing quartz, K-feldspar, garnet, biotite, sillimanite,  $\pm$  rutile,  $\pm$  cordierite (e.g., Cavalcante et al., 2013). Some garnet-bearing leucogranites are almost free of biotite (Figure 6c). Rather than a batholith, the EAU represents the anatectic core of the Araçuaí belt, which was intruded by several late orogenic charnockitic plutons ( $\sim 520$  Ma). This unit is characterized by a widespread, penetrative magmatic fabric marked by a magmatic foliation that dominantly dips gently to moderately in

various directions due to open folds that affected an initial low-angle foliation (Cavalcante et al., 2013). Detailed mapping of magnetic foliations and lineations across the EAU revealed a complex flow field, characterized by a western domain where gently dipping foliations bear lineations that progressively rotate from SW in the south to NW in the north (Figure 2) and by an eastern domain where subvertical NS-trending foliations bear sub-horizontal, orogen-parallel lineations (Cavalcante et al., 2013). The eastern boundary of the anatectic unit is defined by a progressive transition to migmatitic kinzigites (Figure 6d) in which are intercalated layers of orthopyroxene-bearing granulites.

Cavalcante et al. (2014, 2018) using the Ti-in-quartz (TitaniQ), the Zr-in-rutile geothermometers in anatexites and Fe-Mg exchange geothermobarometers in neighbouring kinzigites obtained temperatures of 780-800 °C and pressures in the range of 650-700 MPa; these P-T conditions are interpreted as those under which crystallization of anatexites began during cooling. These thermobarometric estimates are in good agreement with those obtained for the migmatitic kinzigites by Munhá et al. (2005) using Fe-Mg exchange geothermobarometers and, more recently, by Richter et al. (2016) from phase equilibrium modeling. Such P-T conditions are consistent with the presence of cordierite (Harley et al., 2002; Pattison et al., 2003; Harley, 2004) in the studied rocks and also of rutile that, according to Le Breton and Thompson (1988), crystallizes at  $T \geq 760$  °C. Evidence of destabilization of restitic biotites in several samples further supports temperatures  $>800$  °C (Le Breton and Thompson, 1988; Vielzeuf and Holloway, 1988; Pattison et al., 2003). As highlighted by Cavalcante et al. (2014), such high temperatures probably allowed for melt fractions  $>30\%$ , which may have drastically reduced the viscosity of the anatectic middle crust (Rosenberg and Handy, 2005; Vanderhaeghe, 2009). Moreover, the contrast in peak equilibrium temperatures supports a major tectonic contact between the central (CPU) and eastern (EAU) units.

Vaucher et al. (2007) reported a SHRIMP U-Pb zircon age of  $575 \pm 3$  Ma for a diatexite from the EAU. Additional U-Pb SHRIMP zircon ages from anatectic granite, diatexites, and metatexites substantiate a broad variability in U-Pb zircon ages across the EAU (Cavalcante et al., 2018). Several diatexites and anatectic granites yielded ages in the range 597-593 Ma, whereas the remaining anatectic samples were dated between 589 and 572 Ma. Ages are on average slightly older in the northwest and younger in the southeast, but the trend is not clear-cut (Figure 5). Richter et al. (2016) reported a similar age range (595-570 Ma) for samples from the easternmost "Nova Venecia" kinzigitic unit of the Araçuaí belt. These data indicate

that anatexis was already underway in the middle crust (~25 km) of the Araçuaí belt by ~600 Ma and that it remained active until at least 570 Ma (Cavalcante et al., 2018).

### 3. $^{40}\text{Ar}/^{39}\text{Ar}$ ages

Ten samples were collected across the CPU: two synkinematic tonalites from the contact between this domain and the WMU, five synkinematic granodiorites/tonalites from the São Vitor and Galiléia complexes showing a well developed magmatic fabric, one synkinematic leucogranite (Wolf granite), one muscovite-bearing peraluminous granite from the Palmital plutonic body, and one orthogneiss from the country rock (Figure 7). The U-Pb zircon ages of six of the selected plutonic rocks are close to 580 Ma (Mondou et al., 2012). Biotite was separated and analyzed for the 10 samples; amphibole was analyzed in four tonalites, and muscovite in the peraluminous Palmital granite (see Table 1).

Six samples from the EAU were selected among the 12 recently dated by Cavalcante et al. (2018): four anatectic granites, one diatexite and one metatexite (Figure 4, Table 1). Their U-Pb zircon ages range between 597 and 572 Ma. All selected samples display a well-developed magmatic foliation and are free of solid-state deformation (Cavalcante et al., 2013). Only biotite was dated since amphibole was not found in anatexites.

The location of the samples for which  $^{40}\text{Ar}/^{39}\text{Ar}$  ages were obtained in this study is shown on Figure 7, which also integrates  $^{40}\text{Ar}/^{39}\text{Ar}$  ages obtained previously (Table 1, 2 amphibole and 3 biotite ages from Petitgirard et al., 2009). Samples from the CPU were analyzed at Geosciences Montpellier (University of Montpellier, France) and those from the EAU at the Geochronological Research Center of the University of São Paulo (Brazil).  $^{40}\text{Ar}/^{39}\text{Ar}$  diagrams are shown on Figures 9 and 10. Full analytical data are available in the Supplementary Material #3 and #4.

In the CPU,  $^{40}\text{Ar}/^{39}\text{Ar}$  cooling ages on amphibole, muscovite, and biotite show a larger dispersion than the U-Pb ages on zircon; they range from about 550 to 470 Ma (Figure 7). This dispersion reflects both the difference of closure temperatures between amphibole and micas and the variability from sample to sample. Amphiboles from tonalite/granodiorite samples provide nearly undisturbed age spectra with plateau ages ranging from  $549.2 \pm 5.6$  Ma to  $500 \pm 5$  Ma (Figure 8). Biotites from the São Vitor and Galiléia tonalites/granodiorites yielded  $^{40}\text{Ar}/^{39}\text{Ar}$  ages between  $489.5 \pm 5.4$  Ma and  $474.5 \pm 4.4$  Ma; those of the Wolf leucogranite  $491.9 \pm 5.8$  Ma and those from the Palmital granite and one orthogneiss sample overlap at  $484.1 \pm 4.7$  Ma. Muscovite from the Palmital granite yield plateau age of  $487.6 \pm 4.5$  Ma for more than 90% of the released  $^{39}\text{Ar}$  (Figure 8). Two samples of tonalite collected



close to the contact between the WMU and the CPU yield older cooling ages for amphibole ( $549.2 \pm 5.6$  and  $541.6 \pm 7.7$  Ma) and biotite ( $532.2 \pm 5.4$  and  $507.5 \pm 5.3$  Ma). Although these ages are reliable from the analytical point of view, their geological significance remains unclear since for neighboring samples collected on both sides of this contact amphibole and biotite yield younger cooling ages in the range 510-470 Ma.

In the EAU, biotite ages span from  $485.8 \pm 4.4$  Ma to  $458.5 \pm 4.2$  Ma with the oldest age obtained for the northernmost sample and the youngest one for the southernmost sample (Figure 9; Supplementary Material #4). This distribution is correlated with the variation in U-Pb zircon ages across this domain.

## 4. *Discussion*

### 4.1. Origin and duration of the heating episode

Considering the current crustal thickness of ~40 km (Assumpção et al., 2013) and the paleopressures of 0.6-0.7 GPa recorded by rocks currently exposed in the central Araçuaí orogen (Petitgirard et al., 2009; Cavalcante et al., 2014; Richter et al., 2016), the orogenic crustal thickness was likely >60 km. Temperatures of 740 to  $\geq 800$  °C were recorded at 20-25 km depth (Petitgirard et al., 2009; Cavalcante et al., 2014; Richter et al., 2016) suggesting an average thermal gradient >30 °C/km within the upper and middle crust (likely lower in the lower crust). Throughout the orogen, the magmatic bodies are either embedded in metapelitic rocks or formed by local anatexis of metapelitic rocks. This supports that the orogenic middle crust of the Araçuaí belt, down to 25 km depth at least, was mostly composed by metapelites with some amphibolite and quartzite intercalated layers. Although the content in heat-producing elements of these metapelites is not known, such a middle crust likely had a rather high radiogenic heat production, which probably contributed significantly to heating (Clark et al., 2011; Clark et al., 2015). In response to heating, it underwent prograde metamorphic reactions that produced free water favoring extensive partial melting (Weinberg and Hasalová, 2015).

The presence of diorite/gabbros mingled within the granodioritic/tonalitic bodies of the CPU (Figure 5c) indicates that partial melting also affected the underlying mantle (Mondou et al., 2012; Gonçalves et al., 2014). Heating in the lithospheric mantle may be due to enrichment in heat-producing elements resulting from metasomatic reactions (Neves et al., 2008) during pre-orogenic rifting of the lithosphere along the eastern border of the São Francisco craton (Cunningham et al., 1996; Uhlein et al., 2007).

Available U-Pb ages on zircons are remarkably consistent across the various geological units that shape the central part of the Araçuaí orogen. Similar ages have been reported in the northern (Siga Jr et al., 1987) and southern portions of the belt, including its connection with the Ribeira transpressional belt (Silva et al., 2005; Bento dos Santos et al., 2010). Ages obtained in the EAU (Cavalcante et al., 2018) and in the kinzigites that bound it eastwards (Richter et al., 2016; Melo et al., 2017) support that by ~600 Ma the middle/lower crust (0.6-0.7 GPa) of the Araçuaí orogen had reached temperatures ~800 °C and was already partially molten, producing garnet-rich aluminous magmas. Following this metamorphic peak, huge volumes of synkinematic granodioritic/tonalitic magmas were emplaced in the CPU. They systematically display a magmatic fabric that, although variable through the whole CPU, is always consistent with the fabric of the country rock, and their ages are in the range 585-575 Ma independently of the orientation of their magmatic fabric (Mondou et al., 2012). In this plutonic complex, only a few ages older than 600 Ma have been obtained (Silva et al., 2005).

The data support that contractional tectonics and crustal thickening started significantly earlier than 600 Ma. A rough estimate may be obtained based on data from the EAU considering heating rates in the range of 5-20 °C/Myr (Harris et al., 2000 and references therein) or 8-15 °C/Myr, as recently deduced from allanite and monazite dating in the central Alps by Janots et al. (2009). Assuming an initial temperature of ~400 °C at 20-25 km depth (McKenzie et al., 2005), heating up to 800 °C would have required between 27 and 50 Myr. This would imply that deformation producing thickening and prograde metamorphism in the Araçuaí belt started before 630 Myr ago. Such a delay between the initiation of the orogeny and the occurrence of widespread partial melting is in agreement with estimates from models for the southern India developed by Clark et al. (2015). It is also consistent with the time intervals (20-60 Myr) between the initiation of collision and melting of the middle/lower crust under peak metamorphism conditions, estimated for the southern Tibet and the High Himalayas or the Canadian Cordillera (e.g., Vanderhaeghe and Teyssier, 2001b and references therein; Zhang et al., 2004; Guo and Wilson, 2012).

The granodioritic/tonalitic bodies of the CPU yield consistent ages in the range 590-570 Ma. These plutonic units display a magmatic fabric parallel to the solid-state fabric of their country rocks, of the mylonites in the WMU, and of the intermediate kinzigitic unit between the CPU and EAU. This supports synkinematic emplacement of huge volumes of granodioritic and tonalitic magmas in the middle crust (Vauchez et al., 2007; Mondou et al., 2012) during the temperature climax, the magmas likely resulting from partial melting of the

lower crust, with minor contribution from mantle melting, as evidenced from mixing with dioritic and gabbroic magmas (Gonçalves et al., 2014).

Younger ages obtained on several late- and post-collisional granitic bodies (Silva et al., 2002, 2005; Mondou et al., 2012) highlight that magmatic pulses occurred over a very long period of time until, at least, 500 Ma. Among the late magmatic bodies, the "Ibituruna" Syenite in the CPU (U-Pb zircon age of 530 Ma; Petitgirard et al., 2009) and the "Padre Paraíso" charnockitic suite in the EAU (U-Pb zircon ages of ~520 Ma; Noce et al., 2000; Mondou et al., 2012) still have a poorly understood origin. Their compositions imply nevertheless that rather high temperature conditions subsisted in the lower crust and underlying mantle up to these late stages of the evolution of the Araçuaí belt. It is worth noticing that the Ibituruna syenite (~530 Ma) has a magmatic fabric (foliation and lineation) parallel to the solid-state fabric in the surrounding HT mylonites (Petitgirard et al., 2009), whereas the charnockites crosscut the tectonic fabric of the Araçuaí belt (e.g., Oliveira et al., 2000; Mondou et al., 2012). Interestingly, these late magmatic events in the Araçuaí belt are coeval with the main tectono-metamorphic event in the West Congo belt in Angola (Monié et al., 2012) and in the "*Cabo Frio Tectonic Domain*" (Schmitt et al., 2004). They might, therefore, record limited reactivation of the Araçuaí belt in response to the formation of the "Congo-Cabo Frio" belt during the final collision between the African and South American proto-continents at 540-530 Ma.

#### 4.2. Cooling rates

In this section, we will only consider U-Pb and  $^{40}\text{Ar}/^{39}\text{Ar}$  ages obtained by our group (Table 1; Vauchez et al., 2007; Petitgirard et al., 2009; Mondou et al., 2012; Cavalcante et al., 2018; this work), for which the location of samples, the definition of the rock type and, in case of magmatic rocks, the synkinematic or post-kinematic emplacement and absence of solid-state reworking are well known. This choice does not alter the results, since there is a good agreement between the ages obtained in different studies for rocks from the Araçuaí belt.

Since our goal was to estimate the cooling temperature at the regional scale, to define the minimum starting temperature of the cooling path we have used the equilibrium temperatures estimated for the metamorphic country rocks (~750 °C; Petitgirard et al., 2009) and the U-Pb zircon ages of synkinematic magmas in the WMU (577-578 Ma; Petitgirard et al., 2009). For the anatexites of the EAU, we have considered U-Pb zircon ages obtained across the domain (597-570 Ma; Cavalcante et al., 2018) and the maximum temperatures estimated for the anatectic rocks using the Ti-in-Quartz (~800 °C, Cavalcante et al., 2014) and

Zr-in-Rutile thermometers (790 °C, Cavalcante et al., 2018). These temperatures are not necessarily representative of the metamorphic peak conditions, since the magmas were already crystallizing and thus cooling, but they rather provide a robust value for the starting temperatures of the cooling path. Finally, for the youngest anatexites of the EAU (570-578 Ma), we have considered that their Ti-in-Zircon temperatures (720-740 °C; Cavalcante et al., 2018) represent the minimum value of the equilibrium temperature at this time.

Figure 10 summarizes all ages obtained by our group for the Araçuaí belt. Zircon U-Pb ages from synkinematic leucogranites in mylonites from the WMU, granodiorites/tonalites from the CPU, and anatexites from the EAU spread from ~600 Ma to ~570 Ma with a clear concentration around 580 Ma (19/29 ages between 575-585 Ma, 8/29 between 585 and 600 Ma), supporting that the metamorphic peak, partial melting, and tonalitic/granodioritic magmatism occurred during this period of time. To estimate a mean cooling rate, we use the median value of 584 Ma ( $\sigma = 7$ ) calculated based on 27 zircon ages (excluding the late Ibituruna syenite AR-414 and the orthogneiss AR-722). Temperature and pressure estimates support that, by ~600-580 Ma, metamorphic temperature at 20-25 km depth was in the range of 750 °C (WPU, Petitgirard et al., 2009) to  $\geq 800$  °C (EAU; Cavalcante et al., 2014). These values crudely define the minimum starting temperature of the cooling path (Figure 10).

Almost all dated minerals are of magmatic origin, except the recrystallized biotite extracted from orthogneiss AR-722, which has an U-Pb zircon age of  $2103 \pm 11$  Ma (Mondou et al., 2012), but yielded similar  $^{40}\text{Ar}/^{39}\text{Ar}$  age as the magmatic biotites.  $^{40}\text{Ar}/^{39}\text{Ar}$  ages on amphibole and micas record, therefore, cooling through the respective closure temperatures. A first estimate of the cooling rate was obtained considering closure temperatures of  $550 \pm 30$  °C for amphibole (Dahl, 1996),  $400 \pm 20$  °C for muscovite (Harrison et al., 2009), and  $325 \pm 20$  °C for biotite (Harrison et al., 1985). However, for very low cooling rates, the isotopic re-equilibration may continue at temperatures lower than the theoretical closure temperature (Dodson, 1973). We have thus recalculated the closure temperatures for amphibole, muscovite and biotite taking into account the estimated cooling rate (5 °C/Myr for amphibole and 15 °C/Myr for biotite and muscovite) and the grain size (Brandon et al., 1998; McDougall and Harrison, 1999; Braun et al., 2006; Reiners and Brandon, 2006). Depending on grain size, estimated closure temperatures range from 485 to 526 °C for amphibole, 288 to 338 °C for biotite and  $416 \pm 4$  °C for the single analyzed muscovite (Table 1).

Cooling rates inferred for various scenarios are shown on Figure 10:

- The first one (curve 1) is calculated using: 1) average ages computed considering all samples (except the syenite AR-414 and the orthogneiss AR-722 as stated

above), i.e., 584 Ma for U-Pb zircon age, 510 Ma and 487 Ma for  $^{40}\text{Ar}/^{39}\text{Ar}$  amphibole and biotite ages respectively, 2) the average closure temperatures of amphibole (508 °C) and biotite (316 °C). This results in cooling rates of 3.9 °C/Myr with an initial temperature ( $T_i$ ) of 800 °C (curve 1) between 584 and 510 Ma (3.3 °C/Myr with  $T_i = 750$  °C) and of 8.4 °C/Myr between 510 and 487 Ma.

- For the second scenario (curve 2), we excluded the two samples that yielded significantly older amphibole and biotite  $^{40}\text{Ar}/^{39}\text{Ar}$  ages, and used average closure temperatures of 504 °C for amphibole and of 319 °C for biotite. The obtained cooling rates are of 3.5 °C/Myr between 584 and 499 Ma with  $T_i = 800$  °C (2.9 °C/Myr with  $T_i = 750$  °C) and of 9.7 °C/Myr between 499 and 480 Ma.
- Even considering only the oldest ages obtained for amphibole (average: 546 Ma) and biotite (average: 520 Ma), cooling rates still remain low (curve 3): 7.6 °C/Myr between 583 and 546 Ma with  $T_i = 800$  °C (6.3 °C/Myr with  $T_i = 750$  °C). Cooling rates below the closure temperature of amphibole range between 16.1 °C/Myr (with AR-590 biotite age of 532 Ma) and 5.8 °C/Myr (with AR-1057 biotite age of 508 Ma) and 8.7 °C/Myr for the average age of biotites (520 Ma).

Local cooling rates for the EAU can be estimated using biotite  $^{40}\text{Ar}/^{39}\text{Ar}$  ages of the six samples for which Cavalcante et al. (2018) obtained U-Pb zircon ages between 597 and 572 Ma (Table 1; Figures 5, 9). Biotite from these samples yield  $^{40}\text{Ar}/^{39}\text{Ar}$  ages from 486 to 459 Ma and closure temperatures from 307 to 338 °C. Considering the oldest anatectic leucogranites of the EAU (AR-1133; curve 4 on Figure 10), which has U-Pb zircon age of  $597 \pm 3$  Ma and  $^{40}\text{Ar}/^{39}\text{Ar}$  biotite age of  $486 \pm 4$ , the TitaniQ temperature for this unit of  $\sim 800$  °C (Cavalcante et al., 2014) as initial temperature, and 307 °C as the closure temperature of biotite, we obtain an average cooling rate of  $\sim 4.4$  °C/Myr during the  $\geq 110$  Myr that followed the crystallization of zircons. Sample AR-1349, for which an equilibrium temperature of 780-790 °C was estimated using Zr-in-rutile data (Cavalcante et al., 2018), yields U-Pb zircon age of 583 Ma and  $^{40}\text{Ar}/^{39}\text{Ar}$  biotite age of 476 Ma (closure T: 323 °C), pointing to an average cooling rate of  $\sim 4.3$  °C/Myr. For the youngest anatectic sample (AR-1370), the  $^{40}\text{Ar}/^{39}\text{Ar}$  biotite age is 469 Ma with a closure temperature of  $\sim 316$  °C, the U-Pb zircon age is 572 Ma, and a minimum ambient temperature of  $\sim 720$  °C may be assumed from Ti-in-zircon data (Cavalcante et al., 2018). This points to cooling by  $\sim 404$  °C in 103 Myr and, therefore, to an average cooling rate of 3.9 °C/Myr. These cooling rates estimated for the EAU rely on  $^{40}\text{Ar}/^{39}\text{Ar}$  biotite ages and closure temperatures only. They lack intermediate

constraints and therefore consider a linear cooling between the crystallization of zircons and the closure of the K/Ar system in biotite. Taking into account the difference in cooling rates above and below the closure temperature of amphibole obtained for rocks from the WMU and the CPU, a cooling rate significantly lower than 4 °C/Myr may also be expected for the EAU during the first tens of million years after the peak of metamorphism.

In summary, U-Pb,  $^{40}\text{Ar}/^{39}\text{Ar}$  ages and the metamorphic temperature estimates from the three allochthonous units consistently suggest low cooling rates (~3 to 8 °C/Myr; likely 3-5 °C/Myr) during at least the first 40 Myr after initiation of cooling (based on the oldest  $^{40}\text{Ar}/^{39}\text{Ar}$  ages of amphiboles, Am3 on Figure 10), more probably 70-80 Myr (based on the average amphibole  $^{40}\text{Ar}/^{39}\text{Ar}$  age, Am1 on Figure 10), or even >100 Myr in the EAU. These data also imply that cooling was faster (at least 11-15 °C/Myr) after the closure of the amphibole K/Ar system, and possibly even faster (>20 °C/Myr) approaching the closure temperature of muscovite, although this last inference needs further investigation since it relies on the single muscovite age of our database. Moreover, as discussed above, the estimated cooling rates consider linear trends between the different time markers (crystallization of zircon and the closure of  $^{40}\text{Ar}/^{39}\text{Ar}$  system in amphibole and biotite). Yet, cooling was probably lower right after the metamorphic peak, especially during progressive solidification of magmatic rocks, due to the release of the latent heat of crystallization (Michaut and Jaupart, 2011), and has progressively increased through time. However, although no evidence has been found yet, episodes of reheating cannot be ruled out.

The present estimates of cooling rates in the Araçuaí belt are in rather good agreement with those proposed by Bento dos Santos et al. (2010; 2014) for anatexites, granulites, and charnockites from the northern Ribeira belt. These authors propose a two-step thermal evolution with initial cooling rates of 1-5 °C/Myr during 50-90 Myr, followed by faster cooling by 8-30 °C/Myr and possibly up to 100 °C/Myr, based on diffusion of  $\text{Fe}^{2+}$  and Mg between garnet and biotite inclusions. Although the approaches are different, estimates obtained in both areas consistently point to a very slow cooling during several tens of million years after the major high temperature deformation that shaped the Araçuaí and the northern Ribeira belts.

$^{40}\text{Ar}/^{39}\text{Ar}$  ages of 498-493 Ma for amphibole and of 487 to 466 Ma for biotite obtained in the West Congo belt in Angola (Monié et al., 2012) are similar to those obtained in the Araçuaí belt, suggesting that, although the age of the orogenic/metamorphic peak is different in these two belts (Araçuaí : 600-580 Ma; West Congo ~540-530 Ma), they shared a common cooling history after the final amalgamation of Western Gondwana.

### **4.3. Effect of protracted high temperature conditions in the middle crust on its rheology and strain repartition**

Under "hot orogen" conditions (high temperatures and low cooling rates in the middle and lower crust), we may expect specific rheological behaviors. When the temperature gradient reaches equilibrium, it is almost homogeneous over large distances both laterally and vertically (e.g., Whittington et al., 2009). Rheological contrasts between different crustal rock types are minimized, and strain localization efficiency, which is inversely proportional to stress and thus to temperature, becomes much lower. Strain tends to be distributed over large volume of rocks (Vanderhaeghe and Teyssier, 2001b; Vauchez et al., 2007). Consequently, transitions between orogenic domains should be much smoother than under lower temperature conditions (Vanderhaeghe and Teyssier, 2001a). This is particularly true when the middle to lower crust undergoes widespread partial melting, because this process may lead to a decrease in viscosity by several orders of magnitude (e.g., Rosenberg and Handy, 2005; Rosenberg et al., 2007; Cavalcante et al., 2014). The presence of even a small proportion of melt in a rock significantly modifies its viscosity. For instance, Rosenberg and Handy (2005) pointed out through reinterpretation of experimental data on partially molten systems that the strength of a rock undergoes a drastic drop during the first ~7% of partial melting. They also argued that, symmetrically, the strength of magmas deforming during crystallization remains low until they reach a proportion of solid-phase of ~90% and then increases rapidly up to the solidus. When cooling is slow, as it is the case in the Araçuaí orogen, high melt fractions subsist for long times and, by consequence, partially crystallized magmatic bodies or partially molten anatexites may accommodate most of the strain, either gravity-induced or due to far-field forces, during most of the duration of the continental collision.

The three main allochthonous units of the Araçuaí orogen are characterized by the presence of large volumes of synkinematic magmas intermingled with metasedimentary rocks: leucogranites interlayered with mylonites in the western unit, granodiorites/tonalites in the central unit, and anatexites in the eastern unit. Such large volumes of magmas in the middle crust certainly had a major impact on the rheology of the orogenic lithosphere. Using the cooling rates discussed in the previous section, we may roughly estimate the time lapse between emplacement and solidification of the magmas. For instance, the oldest anatectic granite of the EAU, emplaced at ~597 Ma in the middle crust at a minimum temperature of 800 °C yields a mean cooling rate of ~4 °C/Myr, suggesting that the solidus temperature (~630 °C) was attained at least 40-45 Myr after its emplacement, i.e., at about 550-555 Ma. Time lapses in the range of 30-40 Myr are obtained considering the synkinematic

leucogranites of the WMU and the tonalite and granodiorites of the CPU emplaced at ~580 Ma in mylonites or metasediments equilibrated at ~750 °C, which yield cooling rates of 3-4 °C. The consistent estimates for the different units of the Araçuaí belt support that the large volumes of magmas emplaced or formed in the three allochthonous units allowed for magmatic flow and hence maintained low strengths in the middle crust for ~40 Myr after initiation of cooling. Considering the suggestion by Ackerson et al. (2018) that granitic and granodioritic magmas may contain a significant volume of interstitial magma down to temperatures as low as ~500 °C, the above value may be still an underestimate. Indeed, in the Grenville Province in North America, cooling rates in the range 2.3-4.4 °C/Myr and maintenance of supra-solidus conditions over ≥70 Myr have been substantiated (Turlin et al., 2018). The presence today, as deduced from seismic profiles (Nelson et al., 1996), of a partially molten middle crust beneath Tibet, which results from partial melting initiated 20-25 Myr ago (Zhang et al., 2004; Guo and Wilson, 2012), illustrates that a long-lived partially molten crust may have been present in orogens of a variety of ages.

Viscosity increase upon cooling may generate a strength inversion between the magmatic bodies and their country rocks. Nabelek and Liu (2004) suggested, for instance, inversion of shear strength between a mica schist and a dry granite at a temperature of ca. 530 °C depending weakly on strain rate. Based on the cooling rates estimated from our data, strength inversion between metapelitic country rocks and magmatic bodies might have occurred as late as 60 Myr after emplacement of the magmatic bodies. The magmatic bodies were therefore the most deformable part of the middle crust during several tens of million years and, considering their large volume, likely accommodated most of the strain imposed by both plate tectonics and gravity. Upon cooling and crystallization of the magmas, the strength of the magmatic rocks became higher than the strength of the metasedimentary country rocks and the late pulses of deformation must have been accommodated mostly in metasediments.

The viscosity increase during cooling in a hot orogen may also lead to a progressive decrease of the contribution of gravity-driven forces to regional deformation so that the strain regime becomes dependent on far-field forces only. Strengthening of the middle crust may also have allowed more effective transmission of tectonic forces toward the external domains of the orogen, which are, in the present case, the remobilized eastern border of the São Francisco craton.



#### 4.4. Tectonic evolution of the Araçuaí belt

The slow cooling rates estimated in this study and their possible rheological consequences require reconsidering the tectonic evolution of the Araçuaí belt. As stated above, a characteristic of this orogenic segment is that strain was almost evenly distributed across the tectonic units described previously and occurred under high temperature conditions in the presence of syntectonic magmas. However, detailed mapping revealed that the tectonic fabric is variable across the belt. In the CPU and EAU in particular, the foliation and lineation form a complex pattern supporting a 3D deformation (Mondou et al., 2012; Cavalcante et al., 2013). Even if domains with different tectonic fabrics display consistent HT conditions of deformation and similar U-Pb ages of synkinematic magmas, the question of their contemporaneity remains open, since the present study substantiates that HT conditions were maintained during several tens of Myr. In partially molten rocks a new deformation event tends to erase evidence of any previous one. Fast diffusion, allowing for easy grain boundary migration, may have the same effect in HT metamorphic rocks. Under such conditions, it is difficult to establish a reliable chronology since classical techniques of structural analysis are therefore less efficient than in faster cooling orogenic belts.

Interestingly, despite the homogeneity of rock types, equilibrium temperatures, and systematic deformation in the magmatic state throughout the whole EAU, geochronological data denote a diachronous tectonothermal evolution within this unit. There is a correlation between the southeastward decrease in zircon ages evidenced by Cavalcante et al. (2018) and the variation in  $^{40}\text{Ar}/^{39}\text{Ar}$  biotite ages across the EAU. Samples with the oldest U-Pb ages were the first ones to reach the closure temperature of biotite and samples with the youngest U-Pb ages also yield the youngest  $^{40}\text{Ar}/^{39}\text{Ar}$  biotite ages (Figure 11). Only the  $^{40}\text{Ar}/^{39}\text{Ar}$  age of biotite from the anatectic granite AR-535 does not follow this tendency, displaying a younger than expected biotite  $^{40}\text{Ar}/^{39}\text{Ar}$  age. This might be due to the vicinity of a large massif of charnockite emplaced at ~520 Ma. The presence of this hot magmatic body may have reduced the cooling rate in the surrounding rocks during its solidification. There is no evidence of a correlation between U-Pb and Ar/Ar ages in the WMU and CPU, suggesting that the EAU underwent a specific thermotectonic evolution.

The variations in U-Pb and Ar/Ar ages support that, although not far from each other, some parts of the EAU started to crystallize and cooled down well before other parts. This might be due to diachronic migration of granites generated in the anatectic middle crust. However, considering the complex strain pattern mapped across the EAU (Cavalcante et al., 2013), the variation in thermal evolution in the EAU is in good agreement with a "channel-

flow like" deformation during which, due to gravity forces, some parts of the anatectic core of the belt were thrust upwards before or more efficiently than other parts (Cavalcante et al. 2018). The western EAU anatexites, in an initially shallower position, crystallized zircon and reached the closure temperature of biotite before the initially deeper eastern EAU. The regional variation in ages may also mean that the transcurrent fabric mapped in the eastern EAU (Cavalcante et al., 2013; Figure 2) has been formed after the gently-dipping foliations of the western part of the EAU, even if strain was, in both cases, accommodated by magmatic flow in the anatexites.

The "channel-flow like" interpretation for the deformation of the EAU is in agreement with the large-scale structure of the belt and with the crosscutting relationships of the contacts between the different units (Figure 12), which suggest diachronic deformations under supra-solidus temperature across the belt. The anatexites of the EAU cover discordantly the other allochthonous units. In the northernmost part of the Araçuaí belt, they are directly atop the para-autochthonous HT metasediments of the São Francisco craton (Figure 12a), while in the central part of the Araçuaí belt, the EAU is thrust over the subvertical contact between the western CPU and the higher temperature intermediate kinzigitic unit (Figure 12b). This supports earlier thrusting of the intermediate kinzigitic unit over the CPU, then verticalization of the contact and, finally, thrusting of the anatexites of the EAU onto the steeply-dipping structures of the central and intermediate units. No evidence of significant solid-state deformation associated with thrusting of the EAU over the other units has ever been observed in the various EAU anatexites, which are solely characterized by a strong magmatic fabric. This suggests that these events, although diachronic, occurred before full solidification of the magmatic bodies in the different units and that, at all times, deformation was concentrated in the partially molten (or crystallized) rocks.

## 5. *Conclusions*

21 new  $^{40}\text{Ar}/^{39}\text{Ar}$  ages of amphibole, muscovite and biotite from 16 samples collected in the central (CPU) and eastern (EAU) units of the Araçuaí belt, together with  $^{40}\text{Ar}/^{39}\text{Ar}$  and U-Pb ages and P-T data previously published by our group (Vauchez et al., 2007; Petitgirard et al., 2009; Mondou et al., 2012, Cavalcante et al., 2013, 2014, 2018) provides constrains on the thermal history of the middle crust in the central part of the Araçuaí hot orogen. U-Pb zircon ages support that by ~600 Ma the middle to lower crust, heated to temperatures of ~800 °C, was already partially molten and that production of anatectic magmas persisted until ~570 Ma at least (Cavalcante et al., 2018). Most of the granodioritic/tonalitic magmatism of

the CPU, as well as the synkinematic leucogranites within the mylonitic metasediments of the WMU, has been emplaced during this period (Nalini et al., 2000a,b; Noce et al., 2000; Petitgirard et al, 2009; Mondou et al., 2012; Gonçalves et al., 2014).

Altogether these data point to a protracted orogenic evolution marked by:

- Initiation of crustal thickening and heating of the middle crust at about 630 Ma,
- Heating of the middle crust to  $\geq 800$  °C and initiation of pervasive partial melting at ~600 Ma,
- Partial melting remained active until at least ~570 Ma; it affected the middle and lower crust and also the mantle,
- Slow cooling (3-5 °C/Ma) of the middle crust, which reached temperatures of ~500 °C at 510-500 Ma and of ~300 °C at ~480 Ma.
- Magmatic rocks maintained high melt fractions for several tens of Myr (>40 Myr) during which they accommodated most of the imposed deformation by magmatic flow. A rough estimate suggests that they reached the solidus temperature (~630 °C) at ~545-555 Ma.
- The anatexites of the EAU underwent a diachronic evolution: those from the northwestern part crystallized and cooled down earlier than those from the southeastern part. However, estimated cooling rates across the EAU are similar. This diachronic evolution is consistent with a "channel flow like" tectonic model compatible with the 3D deformation of anatexites substantiated by Cavalcante et al. (2013, 2018).

Such a protracted thermal evolution had major effects on the rheology of the orogenic crust, on the strain repartition across the belt, and thus on the tectonic evolution of the Araçuaí belt. During progressive heating of the orogenic crust (prograde metamorphism), deformation was already active and crustal thickening was accommodated in the metasedimentary sequence, but the microstructures recording these early stages of deformation are impossible to differentiate from those formed at the peak of metamorphism in presence of melt and during subsequent deformation under almost stable temperature conditions. Initiation of partial melting at ~600 Ma and syntectonic injection of large volumes of granodioritic/tonalitic magmas between 590 and 570 Ma strongly decreased the viscosity of the middle crust, allowing gravity-induced deformation to combine with far-field compressive forces to produce a 3D deformation regime (Cavalcante et al., 2013). This may explain that northwestwards, the tectonic flow recorded in the middle crust rotate from

661 dominantly eastward onto the São Francisco craton to northward onto the Salvador craton  
662 (e.g., Uhlein et al., 1998).

663 Similar  $^{40}\text{Ar}/^{39}\text{Ar}$  cooling ages are obtained for biotite in both the Araçuaí belt in Eastern  
664 Brazil and the West-Congo belt in Angola (Monié et al., 2012) despite the large differences in  
665 the age of the orogenic climax and in tectonic evolution. This suggests that the late thermal  
666 evolution in the Araçuaí-Ribeira orogeny is shared by the West-Congo - Cabo Frio belt  
667 during the final stages of continental amalgamation. This might explain the late emplacement  
668 of some atypical magmatic bodies (syenites, charnockites) in the Araçuaí belt.

669  
670 **Acknowledgements:** We are indebted to Andréa Tommasi for her critical reading and  
671 commenting of the successive versions of this manuscript. We warmly acknowledge Olivier  
672 Vanderhaegue and an anonymous reviewer for their detailed reviews and their suggestions to  
673 improve our manuscript. We also thank Carolina Cavalcante and Sylvain Petitgirard for their  
674 important contribution to the study of the eastern anatectic and western mylonitic units,  
675 respectively. This study benefited from funding by CAPES-COFECUB project Te 588/07 and  
676 by FAPESP through grant 2005/56372-7. M.H.B.M. Hollanda thanks to CNPq for her  
677 research grant.

- 679 Ackerson, M.R., Mysen, B.O., Tailby, N.D. and Watson, E.B., 2018. Low-temperature  
680 crystallization of granites and the implications for crustal magmatism. *Nature* 559, 94-97.
- 681 Almeida, F.F.M., 1977. O Cráton do São Francisco. *Revista Brasileira de Geociências* 7, 349-  
682 364.
- 683 Assumpção, M., Bianchi, M., Juliá, J., Dias, F.L., Sand França, G., Nascimento, R., Drouet, S.,  
684 Pavão, C.G., Albuquerque, D.F. and Lopes, A.E.V., 2013. Crustal thickness map of  
685 Brazil: Data compilation and main features. *Journal of South American Earth Sciences* 43,  
686 74-85.
- 687 Assumpção, M., Heintz, M., Vauchez, A. and Silva, M.E., 2006. Upper mantle anisotropy in  
688 SE and Central Brazil from SKS splitting: Evidence of asthenospheric flow around a  
689 cratonic keel. *Earth and Planetary Science Letters* 250, 224-240.
- 690 Beaumont, C., Jamieson, R. and Nguyen, M., 2010. Models of large, hot orogens containing a  
691 collage of reworked and accreted terranes. *Canadian Journal of Earth Sciences* 47, 485-  
692 515.
- 693 Bento dos Santos, T.M., Munhá, J.M., Tassinari, C.C.G., Fonseca, P.E. and Dias Neto, C.,  
694 2010. Thermochronology of central Ribeira Fold Belt, SE Brazil: Petrological and  
695 geochronological evidence for long-term high temperature maintenance during Western  
696 Gondwana amalgamation. *Precambrian Research* 180, 285-298.
- 697 Bento dos Santos, T.M., Tassinari, C.C.G. and Fonseca, P.E., 2014. Garnet-biotite diffusion  
698 mechanisms in complex high-grade orogenic belts: Understanding and constraining  
699 petrological cooling rates in granulites from Ribeira Fold Belt (SE Brazil). *Journal of*  
700 *South American Earth Sciences* 56, 128-138.
- 701 Brandon, M.T., Roden-Tice, M.K. and Garver, J.I., 1998. Late Cenozoic exhumation of the  
702 Cascadia accretionary wedge in the Olympic Mountains, northwest Washington State.  
703 *Geological Society of America Bulletin* 110, 985-1009.
- 704 Braun, J., van der Beek, P. and Batt, G., 2006. Quantitative Thermochronology: Numerical  
705 Methods for the Interpretation of thermochronological data. Cambridge University Press,  
706 New York, 272 pp.

709 Cavalcante, G.C.G., Egydio-Silva, M., Vauchez, A., Camps, P. and Oliveira, E., 2013. Strain  
710 distribution across a partially molten middle crust: Insights from the AMS mapping of the  
711 Carlos Chagas Anatexite, Araçuaí belt (East Brazil). *Journal of Structural Geology* 55,  
712 79-100.

713 Cavalcante, G.C.G., Vauchez, A., Merlet, C., Egydio-Silva, M., Bezerra de Holanda, M.H.  
714 and Boyer, B., 2014. Thermal conditions during deformation of partially molten crust  
715 from TitaniQ geothermometry: rheological implications for the anatectic domain of the  
716 Araçuaí belt, eastern Brazil. *Solid Earth* 5, 1223-1242.

717 Clark, C., Fitzsimons, I.C.W., Healy, D. and Harley, S.L., 2011. How Does the Continental  
718 Crust Get Really Hot? *Elements* 7, 235.

719 Clark, C., Healy, D., Johnson, T., Collins, A.S., Taylor, R.J., Santosh, M. and Timms, N.E.,  
720 2015. Hot orogens and supercontinent amalgamation: A Gondwanan example from  
721 southern India. *Gondwana Research* 28, 1310-1328.

722 Cordani, U.G., Ramos, V.A., Fraga, L.M., Cegarra, M., Delgado, I., de Souza, K.G., Gomes,  
723 F.E.M. and Schobbenhaus, C., 2016. Tectonic Map of South America at 1/5 900 000.  
724 CGMW-CPRM-SEGEMAR.

725 Cunningham, W.D., Marshak, S. and Alkmin, F.F., 1996. Structural style of basin inversion at  
726 mid-crustal levels: two transects in the internal zone of the Brasiliano Araçuaí belt, Minas  
727 Gerais, Brazil. *Precambrian Research* 77, 1-15.

728 Dahl, P.S., 1996. The effects of composition on retentivity of argon and oxygen in hornblende  
729 and related amphiboles: A field-tested empirical model. *Geochimica et Cosmochimica*  
730 *Acta* 60, 3687-3700.

731 Dodson, M.H., 1973. Closure temperature in cooling geochronological and petrological  
732 systems. *Contributions to Mineralogy and Petrology* 40, 259-274.

733 Egydio-Silva, M., Vauchez, A., Bascou, J. and Hippertt, J., 2002. High-temperature  
734 deformation in the Neoproterozoic transpressional Ribeira belt, southeast Brazil.  
735 *Tectonophysics* 352, 203-224.

736 Egydio-Silva, M., Vauchez, A., Raposo, M.I.B., Bascou, J. and Uhlein, A., 2005. Deformation  
737 regime variations in an arcuate transpressional orogen (Ribeira belt, SE Brazil) imaged  
738 by anisotropy of magnetic susceptibility in granulites. *Journal of Structural Geology* 27,  
739 1750-1764.

740 Egydio-Silva, M., Vauchez, A., Fossen, H., Gonçalves Cavalcante, G.C. and Xavier, B.C.,  
 741 2018. Connecting the Araçuaí and Ribeira belts (SE – Brazil): Progressive transition from  
 742 contractional to transpressive strain regime during the Brasiliano orogeny. *Journal of*  
 743 *South American Earth Sciences* 86, 127-139.

744 England, P.C. and Thompson, A., 1986. Some thermal and tectonic models for crustal melting  
 745 in continental collision zones. In: M.P. Coward and A.C. Ries (Editors), *Collision*  
 746 *Tectonics*. Geol.Soc.Spec.Pub., pp. 83-94.

747 Gonçalves, L., Farina, F., Lana, C., Pedrosa-Soares, A.C., Alkmim, F. and Nalini Jr, H.A.,  
 748 2014. New U–Pb ages and lithochemical attributes of the Ediacaran Rio Doce magmatic  
 749 arc, Araçuaí confined orogen, southeastern Brazil. *Journal of South American Earth*  
 750 *Sciences* 52, 129-148.

751 Guo, Z. and Wilson, M., 2012. The Himalayan leucogranites: Constraints on the nature of  
 752 their crustal source region and geodynamic setting. *Gondwana Research* 22, 360-376.

753 Harley, S.L., 2004. Extending our understanding of Ultrahigh temperature crustal  
 754 metamorphism. *Journal of Mineralogical and Petrological Sciences* 99, 140-158.

755 Harley, S.L., Thompson, P., Hensen, B.J. and Buick, I.S., 2002. Cordierite as a sensor of fluid  
 756 conditions in high-grade metamorphism and crustal anatexis. *Journal of Metamorphic*  
 757 *Geology* 20, 71-86.

758 Harris, N., Vance, D. and Ayres, M., 2000. From sediment to granite: timescales of anatexis in  
 759 the upper crust. *Chemical Geology* 162, 155-167.

760 Harrison, T.M., Célérier, J., Aikman, A.B., Hermann, J. and Heizler, M.T., 2009. Diffusion of  
 761 <sup>40</sup>Ar in muscovite. *Geochimica et Cosmochimica Acta* 73, 1039-1051.

762 Harrison, T.M., Duncan, I. and McDougall, I., 1985. Diffusion of <sup>40</sup>Ar in biotite:  
 763 Temperature, pressure and compositional effects. *Geochimica et Cosmochimica Acta* 49,  
 764 2461-2468.

765 Hasui, Y., Carneiro, C.D.R. and Coimbra, A.M., 1975. The Ribeira folded belt. *Revista*  
 766 *Brasileira de Geociências* 5, 257-266.

767 Heintz, M., Vauchez, A., Assumpção, M., Barruol, G. and Egydio-Silva, M., 2003. Shear  
 768 Wave Splitting in SE Brazil : an Effect of Active or Frozen Upper Mantle Flow, or both ?  
 769 *Earth and Planetary Science Letters* 211, 79-95.

770 Högdahl, K., Majka, J., Sjöström, H., Nilsson, K.P., Claesson, S. and Konečný, P., 2012.  
 771 Reactive monazite and robust zircon growth in diatexites and leucogranites from a hot,

772 slowly cooled orogen: implications for the Palaeoproterozoic tectonic evolution of the  
 773 central Fennoscandian Shield, Sweden. *Contributions to Mineralogy and Petrology* 163,  
 774 167-188.

775 Holdaway, M.J., Mukhopadhyay, B. and Dutrow, B.L., 1995. Thermodynamic properties of  
 776 stoichiometric staurolite  $\text{H}_2\text{Fe}_4\text{Al}_{18}\text{Si}_8\text{O}_{48}$  and  $\text{H}_6\text{Fe}_2\text{Al}_{18}\text{Si}_8\text{O}_{48}$ , *American*  
 777 *Mineralogist*, pp. 520.

778 Huerta, A.D., Royden, L.H. and Hodges, K.V., 1998. The thermal structure of collisional  
 779 orogens as a response to accretion, erosion, and radiogenic heating. *Journal of*  
 780 *Geophysical Research B: Solid Earth* 103, 15287-15302.

781 Jamieson, R.A., Unsworth, M.J., Harris, N.B.W., Rosenberg, C.L. and Schulmann, K., 2011.  
 782 Crustal Melting and the Flow of Mountains. *Elements* 7, 253-260.

783 Janots, E., Engi, M., Rubatto, D., Berger, A., Gregory, C. and Rahn, M., 2009. Metamorphic  
 784 rates in collisional orogeny from in situ allanite and monazite dating. *Geology* 37, 11-14.

785 Le Breton, N. and Thompson, A.B., 1988. Fluid-absent (dehydration) melting of biotite in  
 786 metapelites in the early stages of crustal anatexis. *Contributions to Mineralogy and*  
 787 *Petrology* 99, 226-237.

788 McKenzie, D., Jackson, J. and Priestley, K., 2005. Thermal structure of oceanic and  
 789 continental lithosphere. *Earth and Planetary Science Letters* 233, 337.

790 McDougall, I. and Harrison, T.M., 1999. *Geochronology and Thermochronology by the*  
 791  $^{40}\text{Ar}/^{39}\text{Ar}$  Method, 2nd edition. Oxford University Press, New York, 269 pp.

792 Melo, M.G., Stevens, G., Lana, C., Pedrosa-Soares, A.C., Frei, D., Alkmim, F.F. and Alkmim,  
 793 L.A., 2017. Two cryptic anatexis events within a syn-collisional granitoid from the  
 794 Araçuaí orogen (southeastern Brazil): Evidence from the polymetamorphic Carlos  
 795 Chagas batholith. *Lithos* 277, 51-71.

796 Michaut, C. and Jaupart, C., 2007. Secular cooling and thermal structure of continental  
 797 lithosphere. *Earth and Planetary Science Letters* 257, 83-96.

798 Michaut, C. and Jaupart, C., 2011. Two models for the formation of magma reservoirs by  
 799 small increments. *Tectonophysics* 500, 34-49.

800 Möller, A., Mezger, K. and Schenk, V., 2000. U-Pb dating of metamorphic minerals: Pan-  
 801 African metamorphism and prolonged slow cooling of high pressure granulites in  
 802 Tanzania, East Africa. *Precambrian Research* 104, 123-146.



803 Mondou, M., Egydio-Silva, M., Vauchez, A., Raposo, M.I.B., Bruguier, O. and Oliveira, A.F.,  
804 2012. Complex, 3D strain patterns in a synkinematic tonalite batholith from the Araçuaí  
805 Neoproterozoic orogen (Eastern Brazil): Evidence from combined magnetic and isotopic  
806 chronology studies. *Journal of Structural Geology* 39, 158-179.

807 Monié, P., Bosch, D., Bruguier, O., Vauchez, A., Rolland, Y., Nsungani, P. and Buta Neto, A.,  
808 2012. The Late Neoproterozoic/Early Palaeozoic evolution of the West Congo Belt of  
809 NW Angola: geochronological (U-Pb and Ar-Ar) and petrostructural constraints. *Terra*  
810 *Nova* 24, 238-247.

811 Morães, R., Nicollet, C., Barbosa, J.S.F., Fuck, R.A. and Sampaio, A.R., 2015. Applications  
812 and limitations of thermobarometry in migmatites and granulites using as an example  
813 rocks of the Araçuaí Orogen in southern Bahia, including a discussion on the tectonic  
814 meaning of the current results. *Brazilian Journal of Geology* 45, 517-539.

815 Morisset, C.-E., Scoates, J.S., Weis, D. and Friedman, R.M., 2009. U-Pb and  $^{40}\text{Ar}/^{39}\text{Ar}$   
816 geochronology of the Saint-Urbain and Lac Allard (Havre-Saint-Pierre) anorthosites and  
817 their associated Fe-Ti oxide ores, Québec: Evidence for emplacement and slow cooling  
818 during the collisional Ottawa orogeny in the Grenville Province. *Precambrian Research*  
819 174, 95-116.

820 Nabelek, P.I. and Liu, M., 2004. Petrologic and thermal constraints on the origin of  
821 leucogranites in collisional orogens. *Transactions of the Royal Society of Edinburgh:*  
822 *Earth Sciences* 95, 73-85.

823 Nabelek, P.I., Whittington, A.G. and Hofmeister, A.M., 2010. Strain heating as a mechanism  
824 for partial melting and ultrahigh temperature metamorphism in convergent orogens:  
825 Implications of temperature-dependent thermal diffusivity and rheology. *Journal of*  
826 *Geophysical Research* 115, B12417.

827 Nalini, H.A., Bilal, E. and Correia Neves, J.M., 2000a. Syn-collisional peraluminous  
828 magmatism in the Rio Doce region: mineralogy, geochemistry and isotopic data of the  
829 neoproterozoic Urucum suite (eastern Minas Gerais state, Brazil). *Revista Brasileira de*  
830 *Geociências* 30, 120-125.

831 Nalini, H.A., Bilal, E., Paquette, J.-L., Pin, C. and Machado, R., 2000b. Géochronologie U-Pb  
832 et géochimie isotopique Sr-Nd des granitoïdes néoprotérozoïques des suites Galiléia et  
833 Urucum, vallée du Rio Doce, Sud-Est du Brésil. *Comptes Rendus de l'Académie des*  
834 *Sciences - Series IIA - Earth and Planetary Science* 331, 459-466.

835 Nalini, H.A., Machado, R. and Bilal, E., 2015. Petrogênese e tectônica da suíte granítica  
836 Urucum, Vale do Rio Doce (Minas Gerais – Brasil): um exemplo de magmatismo sin- a  
837 tardi-colisional associado a zonas de cisalhamento direcionais de alto ângulo. *Brazilian*  
838 *Journal of Geology* 45, 127-141.

839 Narduzzi, F., Farina, F., Stevens, G., Lana, C. and Nalini, H.A., 2017. Magmatic garnet in the  
840 Cordilleran-type Galiléia granitoids of the Araçuaí belt (Brazil): Evidence for  
841 crystallization in the lower crust. *Lithos* 282, 82-97.

842 Nelson, K.D., Zhao, W., Brown, L.D., Kuo, J., Che, J., Liu, X., Klemperer, S.L., Makovsky,  
843 Y., Meissner, R., Mechie, J., Kind, R., Wenzel, F., Ni, J., Nabelek, J., Chen, L., Tan, H.,  
844 Wei, W., Jones, A.G., Booker, J., Unsworth, M., Kidd, W.S.F., Hauck, M., Alsdorf, D.,  
845 Ross, A., Cogan, M., Wu, C., Sandvol, E.A. and Edwards, M., 1996. Partially molten  
846 middle crust beneath southern Tibet; synthesis of Project INDEPTH results. *Science* 274,  
847 1684-1688.

848 Neves, S.P., Tommasi, A. and Vauchez, A., 2008. Intraplate continental deformation:  
849 Influence of a heat-producing layer in the lithospheric mantle. *Earth and Planetary*  
850 *Science Letters*.

851 Noce, C.M., Macambira, M.J.B. and Pedrosa Soares, A.C., 2000. Chronology of  
852 neoproterozoic-cambrian granitic magmatism in the Araçuaí belt, eastern Brazil, based  
853 on single zircon evaporation dating. *Revista Brasileira de Geociências* 30, 20-29.

854 Oliveira, M.-J.R., Pinto, C.P., Féboli, W.L. and Alves dos Santos, R., 2000. Projeto Leste -  
855 Relatório mapa integrado 1:500.000 - Geologia estrutural e tectônica, CPRM - COMIG,  
856 Belo Horizonte.

857 Pattison, D.R.M., Chacko, T., Farquhar, J. and McFarlane, C.R.M., 2003. Temperatures of  
858 Granulite-facies Metamorphism: Constraints from Experimental Phase Equilibria and  
859 Thermobarometry Corrected for Retrograde Exchange. *Journal of Petrology* 44, 867-900.

860 Pedrosa-Soares, A.C., Noce, C.M., Alkmim, F.F.d., Silva, L.C.d., Babinski, M., Cordani, U.  
861 and Castañeda, C., 2007. Orógeno Araçuaí: síntese do conhecimento 30 anos após  
862 Almeida 1977. *Geonomos* 15, 1-16.

863 Petitgirard, S., Vauchez, A., Egydio-Silva, M., Bruguier, O., Camps, P., Monié, P., Babinski,  
864 M. and Mondou, M., 2009. Conflicting structural and geochronological data from the  
865 Ibituruna quartz-syenite (SE Brazil): Effect of protracted "hot" orogeny and slow cooling  
866 rate? *Tectonophysics* 477, 174-196.

867 Peucat, J.J., Ménot, R.P., Monnier, O. and Fanning, C.M., 1999. The Terre Adélie basement  
868 in the East-Antarctica Shield: geological and isotopic evidence for a major 1.7Ga thermal  
869 event; comparison with the Gawler Craton in South Australia. *Precambrian Research* 94,  
870 205-224.

871 Reiners, P.W. and Brandon, M.T., 2006. Using thermochronology to understand orogenic  
872 erosion. *Annual Review of Earth and Planetary Sciences* 34, 419-466.

873 Richter, F., Lana, C., Stevens, G., Buick, I., Pedrosa-Soares, A.C., Alkmim, F.F. and Cutts, K.,  
874 2016. Sedimentation, metamorphism and granite generation in a back-arc region: Records  
875 from the Ediacaran Nova Venécia Complex (Araçuaí Orogen, Southeastern Brazil).  
876 *Precambrian Research* 272, 78-100.

877 Rosenberg, C.L. and Handy, M.R., 2005. Experimental deformation of partially melted  
878 granite revisited; implications for the continental crust. *Journal of Metamorphic Geology*  
879 23, 19-28.

880 Rosenberg, C.L., Medvedev, S. and Handy, M.R., 2007. On the effects of melting on  
881 continental deformation and faulting. In: M. Handy, G. Hirth and N. Hovius (Editors),  
882 *Tectonic Faults: Agents of Change on a Dynamic Earth*. Dahlem Workshop Report, MIT  
883 Press, pp. 357-402.

884 Schmitt, R.S., Trouw, R.A.J., Van Schmus, W.R. and Pimentel, M.M., 2004. Late  
885 amalgamation in the central part of West Gondwana: new geochronological data and the  
886 characterization of a Cambrian collisional orogeny in the Ribeira Belt (SE Brazil).  
887 *Precambrian Research* 133, 29–61.

888 Siga Jr, O., Cordani, U.G., Basei, M.A.S., Teixeira, W., Kawashita, K. and Van Schmus,  
889 W.R., 1987. Contribuição ao estudo geológico e geocronológico da porção nordeste de  
890 Minas Gerais, Anais. IV Simpósio de Geologia de Minas Gerais, pp. 29-44.

891 Silva, L.C., Armstrong, R., Noce, C.M., Carneiro, M.A., Pimentel, M.M., Pedrosa-Soares,  
892 A.C., Leite, C.A., Vieira, V.S., Silva, M.A., Paes, V.J.C. and Cardoso Filho, J.M., 2002.  
893 Reavaliação da evolução geológica em terrenos pré-cambrianos brasileiros com base em  
894 novos dados U-Pb Shrimp, parte II: Orógeno Araçuaí, cinturão mineiro e cráton São  
895 Francisco meridional. *Revista Brasileira de Geociências* 32, 513–528.

896 Silva, L.C., McNaughton, N.J., Armstrong, R., Hartmann, L.A. and Fletcher, I.R., 2005. The  
897 Neoproterozoic Mantiqueira Province and its African connections; a zircon-based U/Pb

898 geochronologic subdivision for the Brasiliano/Pan-African systems of orogens.  
899 Precambrian Research 136, 203-240.

900 Trompette, R., Uhlein, A., da Silva, M.E. and Karmann, I., 1992. The Brasiliano São  
901 Francisco craton revisited (central Brazil). Journal of South American Earth Sciences 6,  
902 49-57.

903 Turlin, F., Deruy, C., Eglinger, A., Vanderhaeghe, O., André - Mayer, A.S., Poujol, M.,  
904 Moukhsil, A. and Solgadi, F., 2018. A 70 Ma record of suprasolidus conditions in the  
905 large, hot, long - duration Grenville Orogen. Terra Nova 30, 233-243.

906 Uhlein, A., Egydio-Silva, M., Bouchez, J.L. and Vauchez, A., 1998. The Rubim Pluton  
907 (Minas Gerais, Brazil): a petrostructural and magnetic fabric study. Journal of South  
908 American Earth Sciences 11, 179-189.

909 Uhlein, A., Trompette, R.R., Egydio-Silva, M. and Vauchez, A., 2007. A glaciação sturtiana  
910 (~750 ma), a estrutura do rifte Macaúbas-Santo Onofre e a estratigrafia do grupo  
911 Macaúbas, faixa Araçuaí. Geonomos 15-1, 106.

912 Vanderhaeghe, O., 2009. Migmatites, granites and orogeny: Flow modes of partially-molten  
913 rocks and magmas associated with melt/solid segregation in orogenic belts.  
914 Tectonophysics 477, 119-134.

915 Vanderhaeghe, O., Medvedev, S., Fullsack, P., Beaumont, C. and Jamieson, R.A., 2003.  
916 Evolution of orogenic wedges and continental plateaux: insights from crustal thermal–  
917 mechanical models overlying subducting mantle lithosphere. Geophysical Journal  
918 International 153, 27-51.

919 Vanderhaeghe, O. and Teyssier, C., 2001a. Crustal-scale rheological transitions during late-  
920 orogenic collapse. Tectonophysics 335, 211-228.

921 Vanderhaeghe, O. and Teyssier, C., 2001b. Partial melting and flow of orogens.  
922 Tectonophysics 342, 451-472.

923 Vauchez, A., Tommasi, A. and Egydio-Silva, M., 1994. Self-indentation of continental  
924 lithosphere. Geology 22, 967-970.

925 Vauchez, A., Egydio-Silva, M., Babinski, M., Tommasi, A., Uhlein, A. and Liu, D., 2007.  
926 Deformation of a pervasively molten middle-crust: Insights from the neoproterozoic  
927 Araçuaí-Ribeira orogen (SE Brazil). Terra Nova 19, 278-286.

928 Vauchez, A., Tommasi, A. and Mainprice, D., 2012. Faults (shear zones) in the Earth's mantle.  
929 Tectonophysics 558-559, 1-27.

- 930 Vielzeuf, D. and Holloway, J.R., 1988. Experimental determination of the fluid-absent  
931 melting relations in the pelitic system. *Contributions to Mineralogy and Petrology* 98,  
932 257-276.
- 933 Weinberg, R.F. and Hasalová, P., 2015. Water-fluxed melting of the continental crust: A  
934 review. *Lithos* 212, 158-188.
- 935 Whittington, A.G., Hofmeister, A.M. and Nabelek, P.I., 2009. Temperature-dependent  
936 thermal diffusivity of the Earth's crust and implications for magmatism. *Nature* 458,  
937 319-321.
- 938 Zeck, H.P., Monié, P., Villa, I.M. and Hansen, B.T., 1992. Very high rates of cooling and  
939 uplift in the Alpine belt of the Betic Cordilleras, southern Spain. *Geology* 20, 79-82.
- 940 Zhang, H., Harris, N., Parrish, R., Kelley, S., Zhang, L., Rogers, N., Argles, T. and King, J.,  
941 2004. Causes and consequences of protracted melting of the mid-crust exposed in the  
942 North Himalayan antiform. *Earth and Planetary Science Letters* 228, 195-212.

Sample number and type	U/Pb <i>Myr</i> (*= <sup>207</sup> Pb/ <sup>206</sup> Pb)	<sup>40</sup> Ar/ <sup>39</sup> Ar <i>Myr</i>			Closing T °C			Cooling rate °C/My
	<i>Zr</i>	<i>Am</i>	<i>Bt</i>	<i>Ms</i>	<i>Am</i>	<i>Bt</i>	<i>Ms</i>	
western mylonitic unit	<i>All data from (1)</i>							
AR-684 leucocratic melt	577±9							
AR-935 leucocratic melt	578±3*							
AR-562 Mylonite		501±5	474±5		488±7	310±11		~3/8
AR-86 leucocratic melt			468±4			318±12		
AR-414 Ibituruna syenite	530±1	505±5			485±6			
<b>Contact zone Derribadinha</b>	<i>All data from (2)</i>	This work						
AR-264 Tonalite	581±4							
AR-590 Tonalite		549±6	532±5		513±7	288±9		7/13
AR-940 leucocratic melt	587±5							
AR-87 leucocratic melt	579±8							
AR-1057 Tonalite	583±4*	542±8	508±5		521±8	293±8		5.6/6.6
<b>Central plutonic unit</b>	<i>All data from (2)</i>	<i>This work</i>						
AR-1009 SV To/Gd		501±9	490±5		526±6	321±9		
AR-800 SV To/Gd	582±6*		485±5			320±10		4.4
AR-968 SV To/Gd	585±7							
AR-957 Wolf leucogranite	585±4		492±6			326±5		4.6
AR-787 Galiléia To/Gd	582±6							
AR-705 Galiléia To/Gd	579±4		475±4			311±9		4.4
AR-815 Galiléia To/Gd	583±4							
AR-717 Galiléia To/Gd	581±4*	500±5	481±5		517±4	311±9		2.9/12
AR-747 Galiléia To/Gd			482±4			325±6		
AR-722 orthogneiss	2103±11		484±5			307±5		
AR-648 Palmital granite			484±5	488±5		306±6	416±4	M-B:27
<b>Eastern anatectic unit</b>	<i>All data from (3) except AR548</i>	<i>This work</i>						
AR-408 Diatexite	597±8							
AR-455 Anatectic granite	594±4							
AR-1133 Anatectic granite	597±3		486±4			307±5		4.4
AR-1145 Diatexite	593±3		477±4			328±3		4.1
AR-1315 Anatectic granite	597±4							
AR-664 Anatectic granite	589±6		474±4			307±5		4.1
AR- 1349 metatexite	583±5		476±4			323±3		4.3
AR-1358 Anatectic granite	585±4							
AR-535 Anatectic granite	575±3		459±4			338±7		3.3
AR-1119 Diatexite	578±4							
AR-1332 Anatectic granite	572±9							
AR-548 Anatectic granite	575±4 (4)		472±4 (1)			315±5		3.9
AR-1370 Anatectic granite	572±4		469±4			316±4		3.9

Table 1: Summary of U-Pb and <sup>40</sup>Ar/<sup>39</sup>Ar ages obtained from rocks collected in the Central Arauaí belt. Samples are organized from West to East. (1) is for ages published in Petitgirard et al. (2009), (2) for those published in Mondou et al., (2012), (3) for those

published in Cavalcante et al., 2018 and (4) for those published in Vauchez et al., 2007. The last column shows individual cooling rates calculated for samples for which U-Pb and  $^{40}\text{Ar}/^{39}\text{Ar}$  ages of amphibole and/or biotite have been obtained, and for which an initial temperature of the country-rock may be inferred (for sample AR-562 and AR-590 an age of 578 Ma and 582 Ma respectively has been assumed taking into account their vicinity and similarity with dated samples). Cooling rates are indicated as: above closing T of amphibole/ between amphibole and biotite closing T. For sample AR-648, MB is for cooling rate between muscovite and biotite closing T.

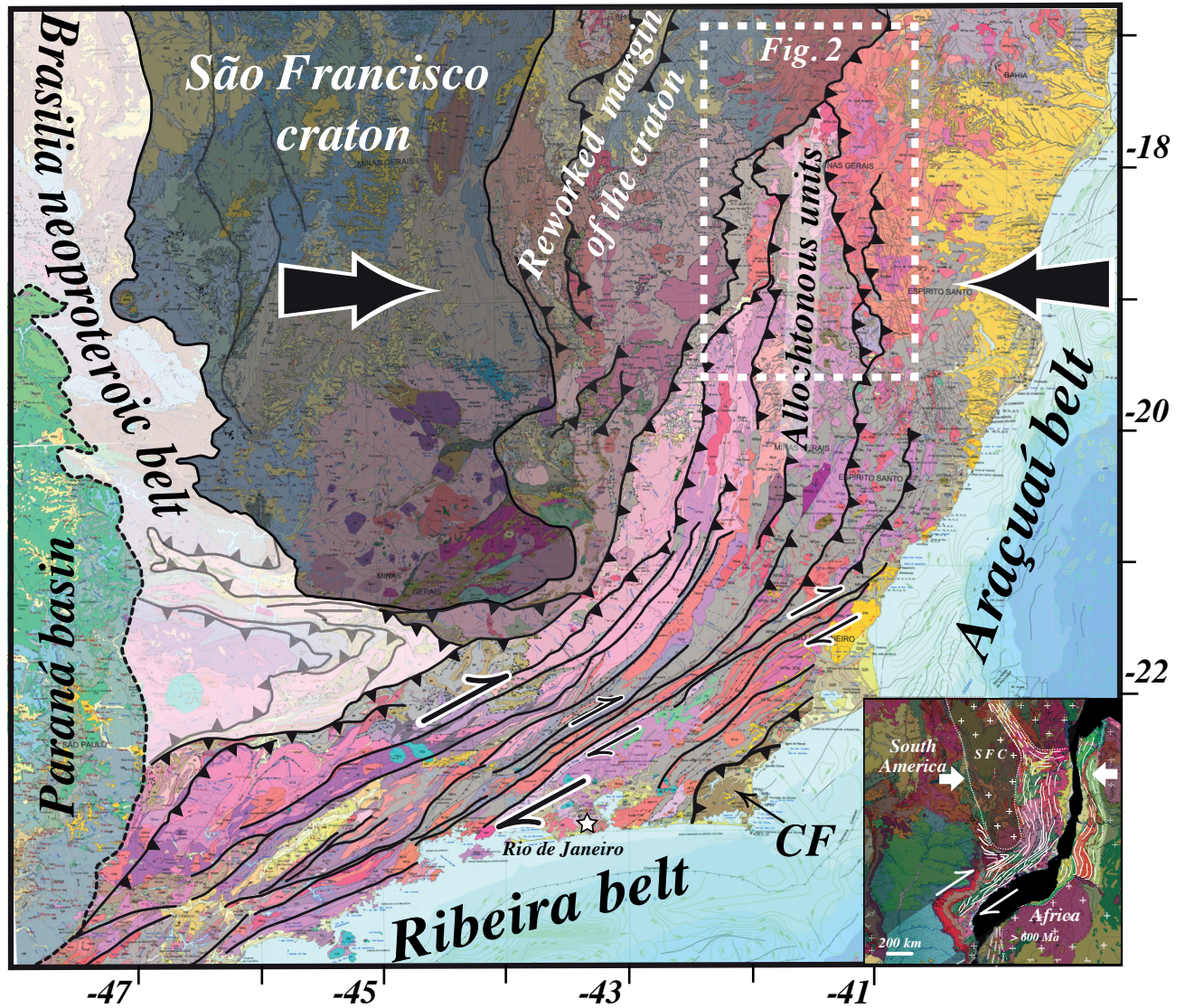


Figure 1: Schematic map of the neoproterozoic tectonic belts in eastern Brazil. The Brasília belt is docked against the western and southwestern boundaries of the São Francisco (SF) craton. The Araçuaí and Ribeira belts formed along the eastern and southeastern boundary of the craton. The transition between these two orogenic segments, marked by a clear change in tectonic regime from contractional to tranpressional, is correlated with the southern termination of the craton. The eastern part of the São Francisco craton was strongly remobilized during the formation of the Araçuaí belt. Deformation in the Cabo Frio tectonic domain (CF) is younger than in the Araçuaí-Ribeira belt and likely represents the westernmost part of the early Cambrian Angola-Congo orogen. The underlying tectonic map is from (Cordani et al., 2016). The area delimited by dotted white lines shows the location of Figure 2. Insert at the lower right corner is a reconstitution of the Ribeira-Araçuaí and Congo orogens before the South Atlantic opening (Vauchez et al., 2007).



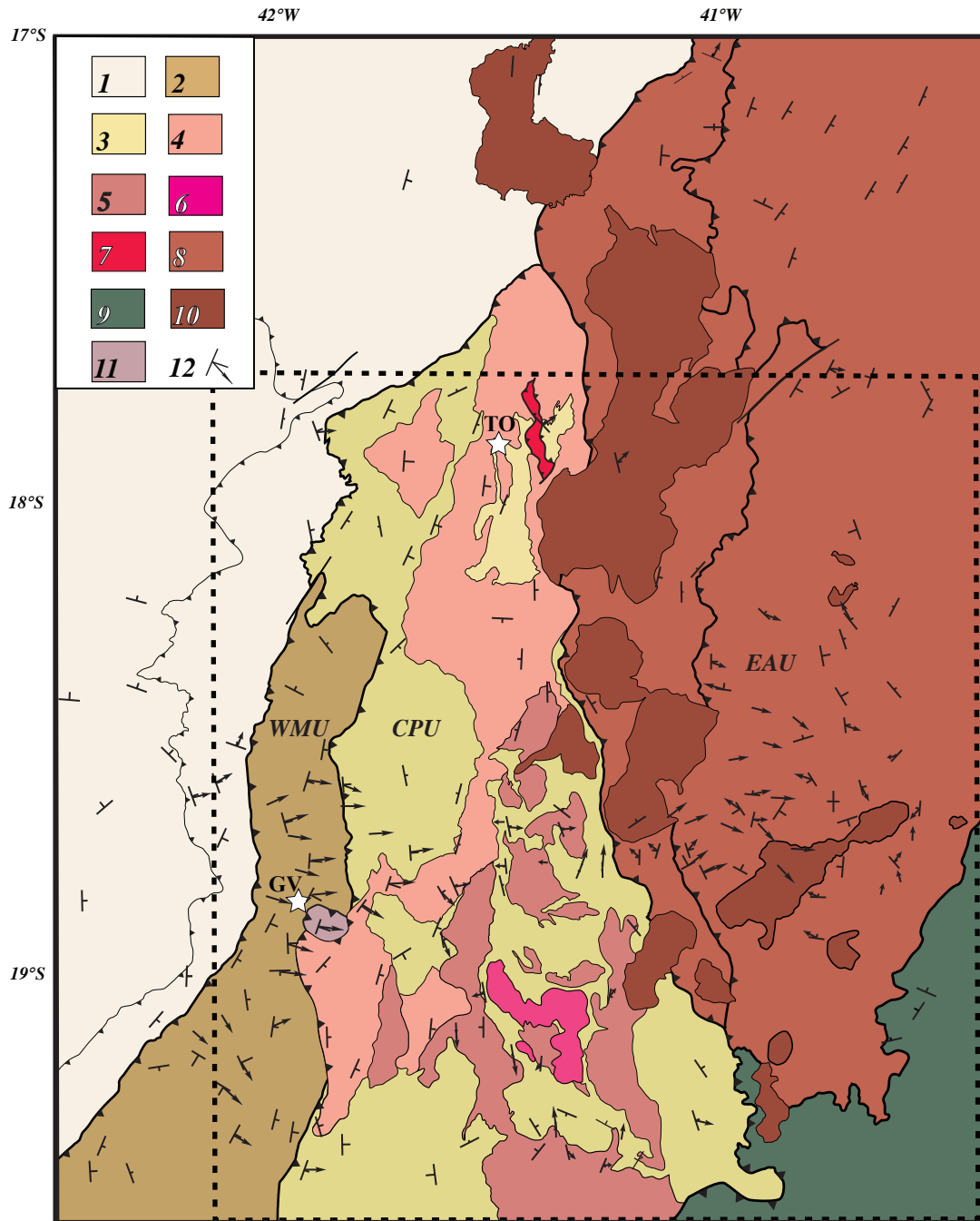


Figure 2: Simplified map of the central Araçuaí belt modified from Vauchez et al., 2007 showing (1) the para-autochthonous cover of the São Francisco cratons and the three allochthonous units: the western mylonitic unit (WMU, 2), the Central Plutonic Unit (CPU, 3-7) and the Eastern Anatectic Unit (EAU, 8-9). In the CPU, (3) is for metasediments, (4) for the "São Vitor" tonalite/granodiorite, (5) for the "Galiléia" tonalite/granodiorite, (6) for the "Palmital" aluminous granite, (7) for the "Wolff" leucogranite. In the EAU: (8) anatexites and (9) kinzigites. (10) is the late "Padre Paraíso" charnockite. (11) foliation and lineation either measured in the field or inferred from AMS (Petitgirard et al., 2009; Mondou et al., 2012; Cavalcante et al., 2013).

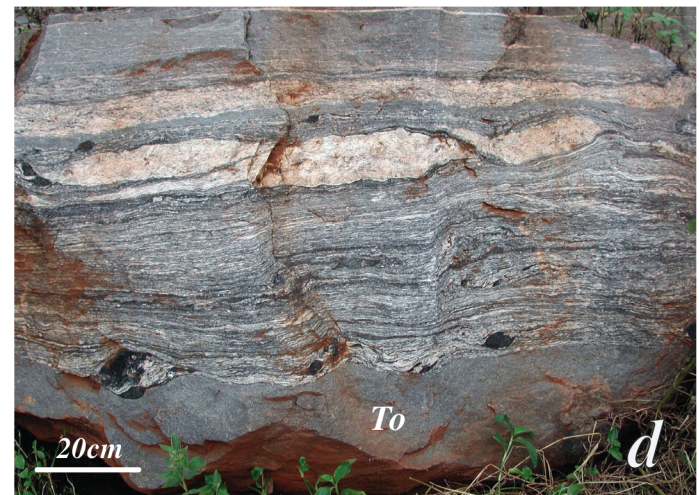
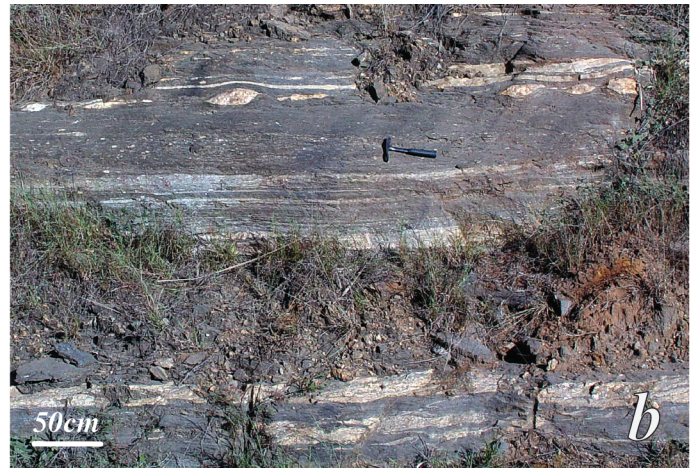


Figure 3: Typical outcrops of the Western Mylonitic Unit (a-c) and of its boundary with the Central Plutonic Unit (d). For the four pictures West is on the right. a-c show metasediments injected by leucocratic granite and shear criteria that indicate top-to-west sense of shear. In (a) lenses are leucogranite. (d) shows intercalations of leucogranite, migmatitic metasediments, tonalite (To) free of solid-state deformation and several asymmetric black lenses resulting from the disruption of an amphibolite layer.

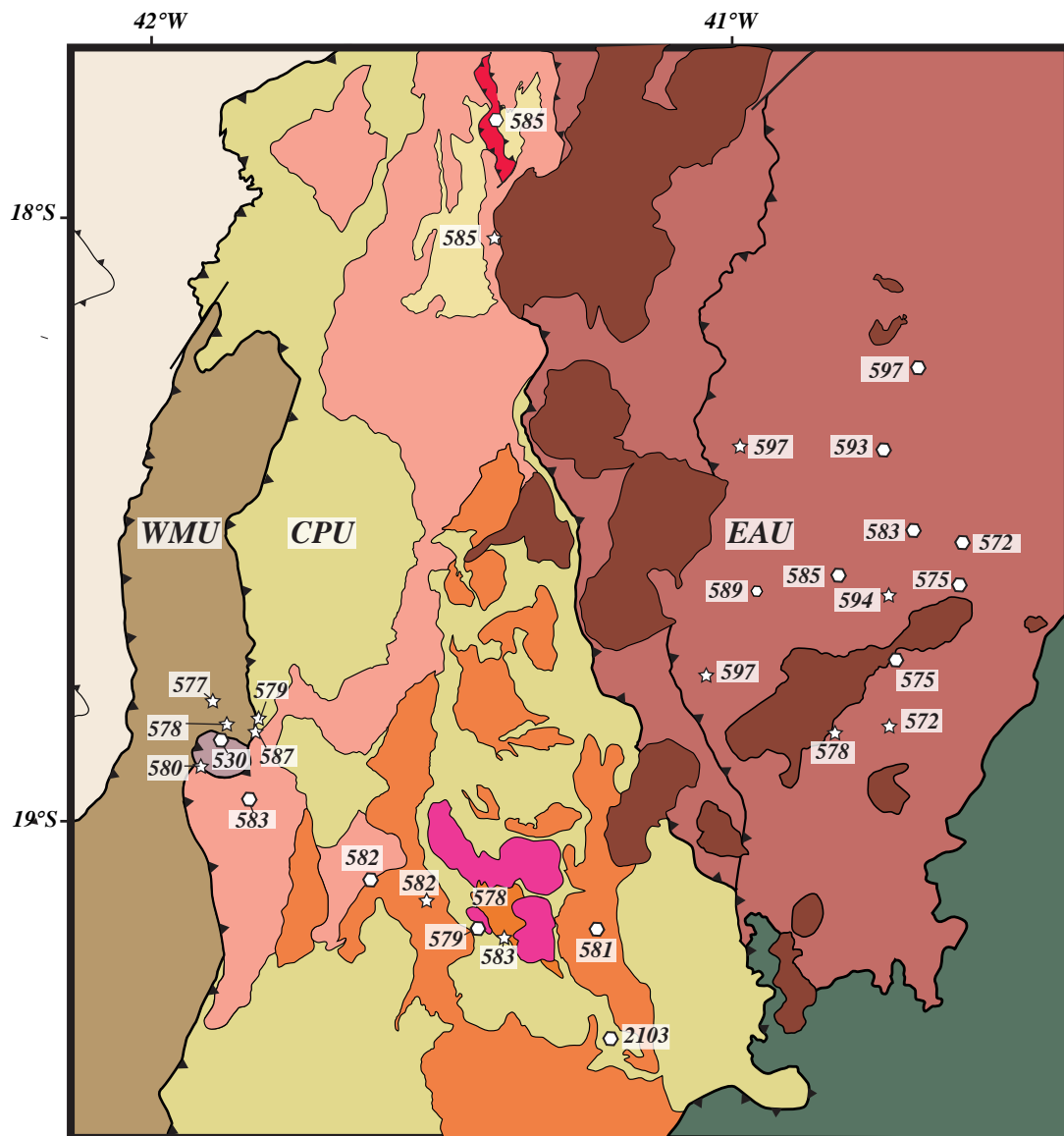


Figure 4: Location and U-Pb ages (Ma) of zircons used in this study. Results (and references) are summarized in table 1.





Figure 5: Pictures of outcrops typical of the Central Plutonic Unit. Tonalites/Granodiorites showing a well-developed magmatic foliation, gently-dipping in the western CPU (a-b) and that progressively becomes subvertical eastward (c-d). In (c) the subvertical magmatic foliation is underlined by elongated dioritic lenses and in (d) by lenses and discontinuous layers of biotite rich granite.



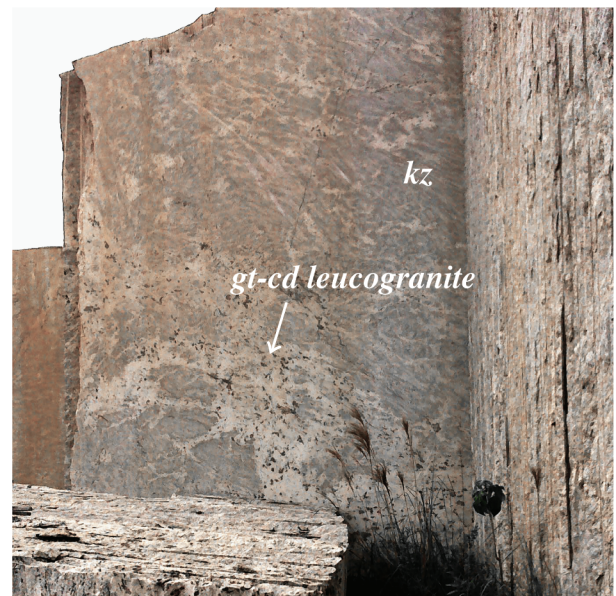
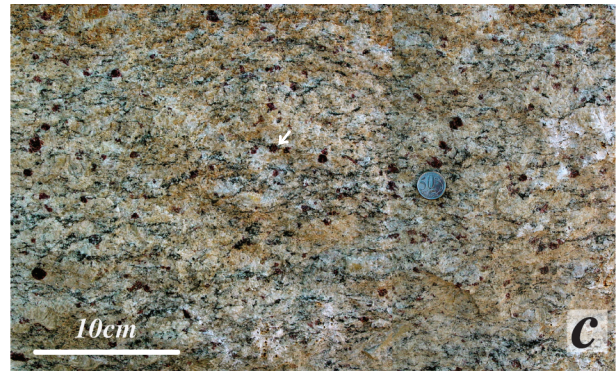
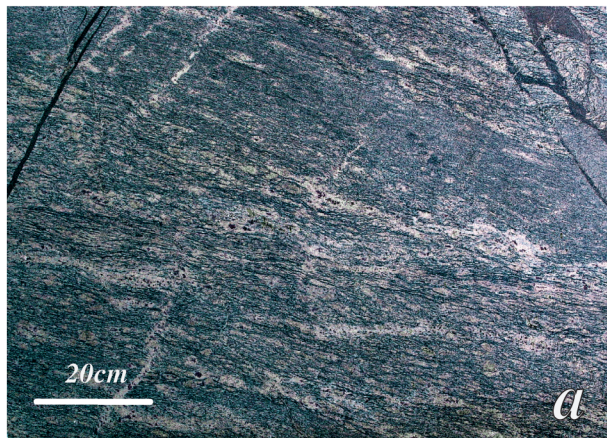


Figure 6: Pictures of outcrops typical of the Eastern Anatectic Unit: metatexites (a), diatexites (b) and garnet-rich leucocratic granite (c), all displaying a well-developed foliation, which is magmatic in the leucosome and solid-state in the restitic parts (when present). (d) shows the anatectic kinzigites (kz) at the eastern boundary of the EAU, in which leucogranitic melt focus and forms lenses and veins. Dark lenses in the leucogranite contains garnet + biotite  $\pm$  cordierite.

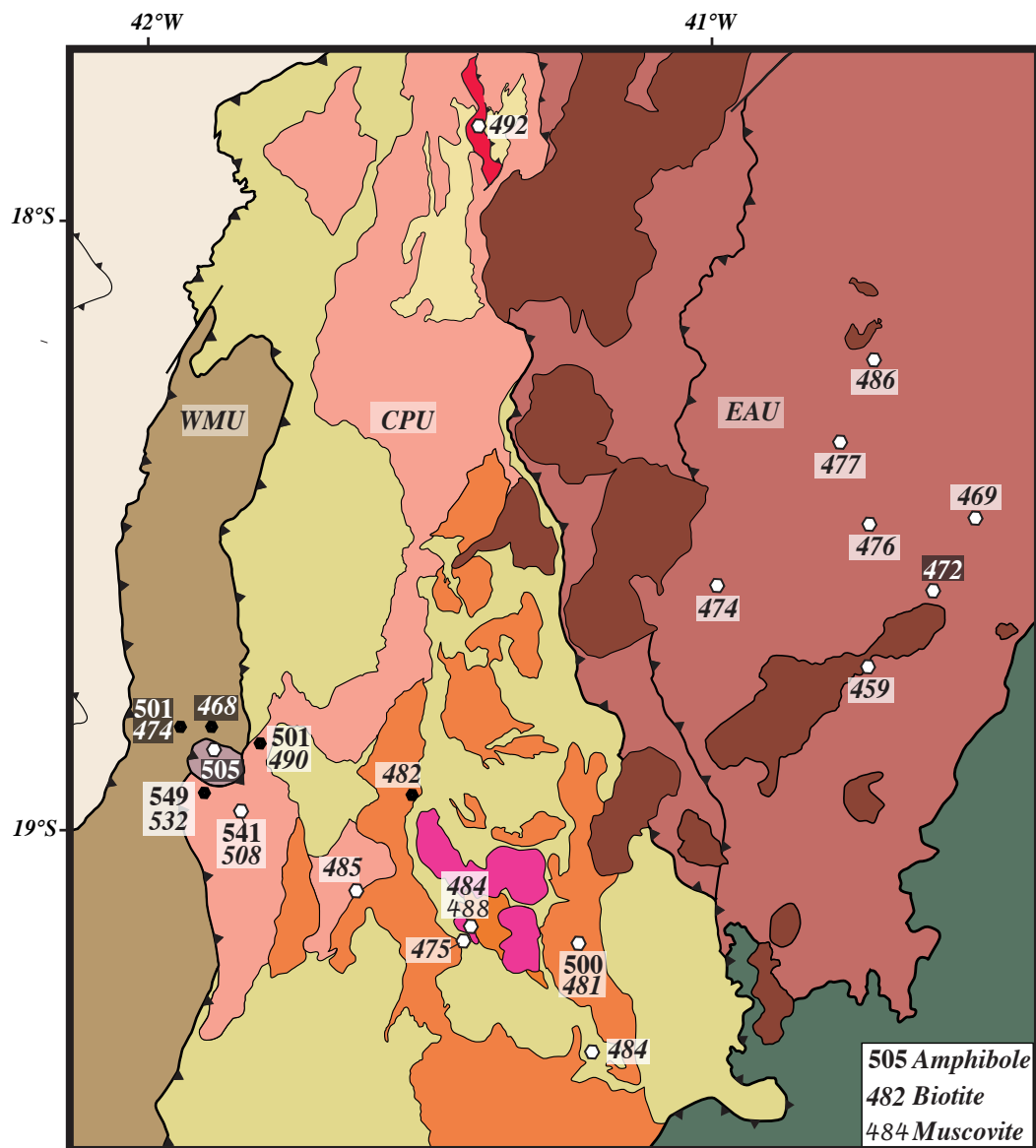
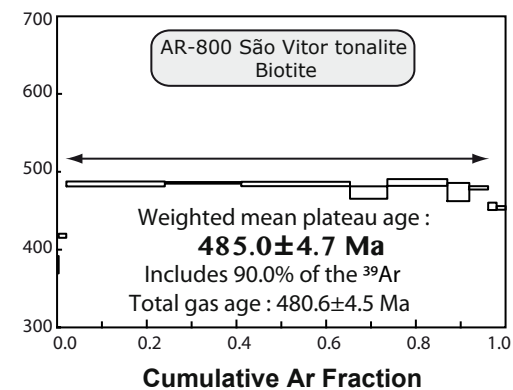
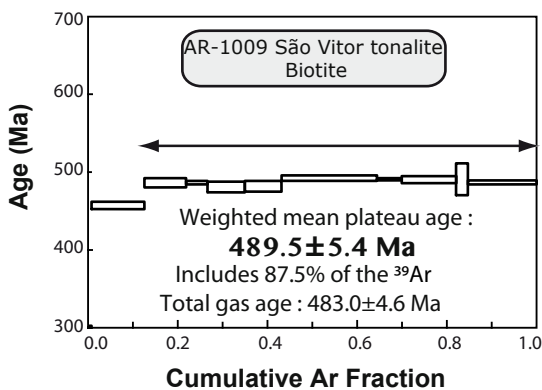
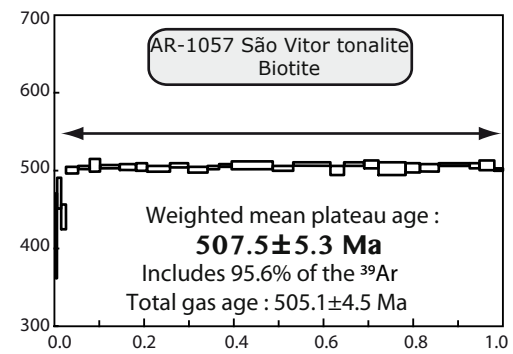
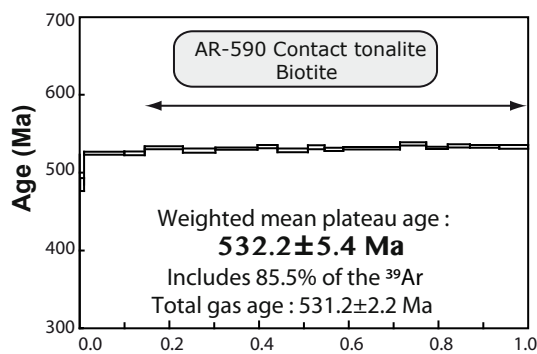
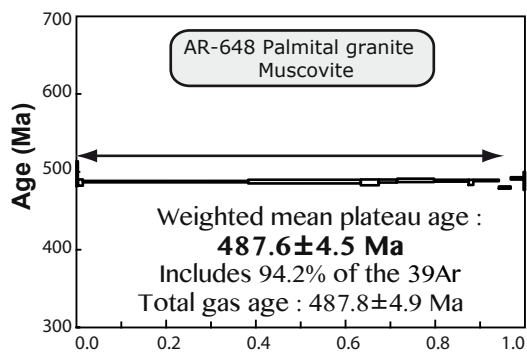
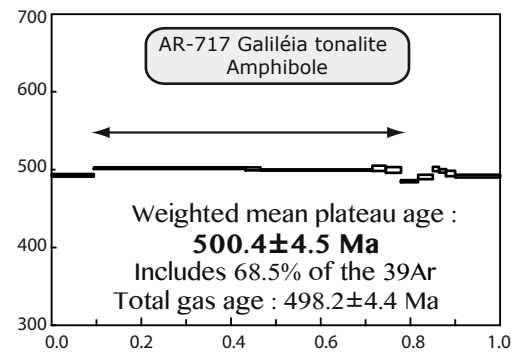
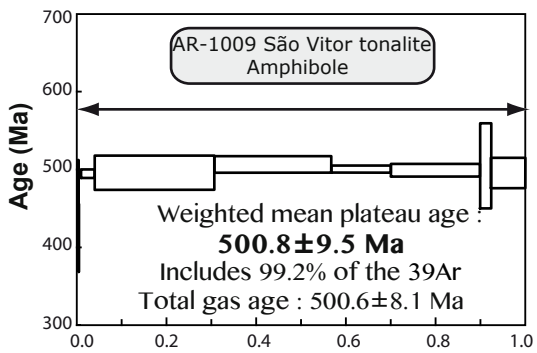
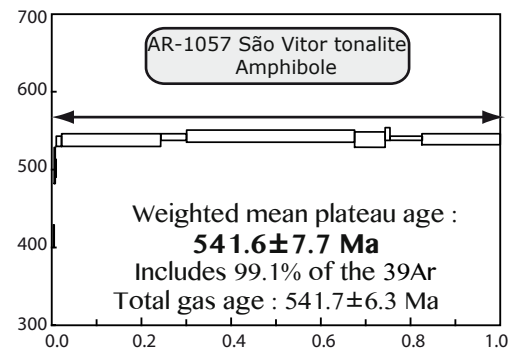
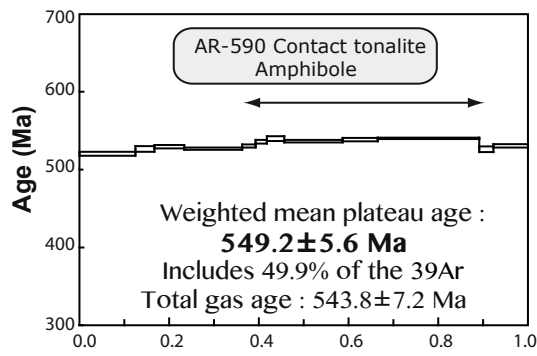


Figure 7 : Location and  $^{40}\text{Ar}/^{39}\text{Ar}$  ages of amphibole, biotite and muscovite used in this study. Numbers in black are ages obtained in this study and those in white are previously published  $^{40}\text{Ar}/^{39}\text{Ar}$  ages (4 samples). Diagrams for newly dated samples are shown on Figures 8 and 9. Analytical data are available in supplementary material #3 and #4.



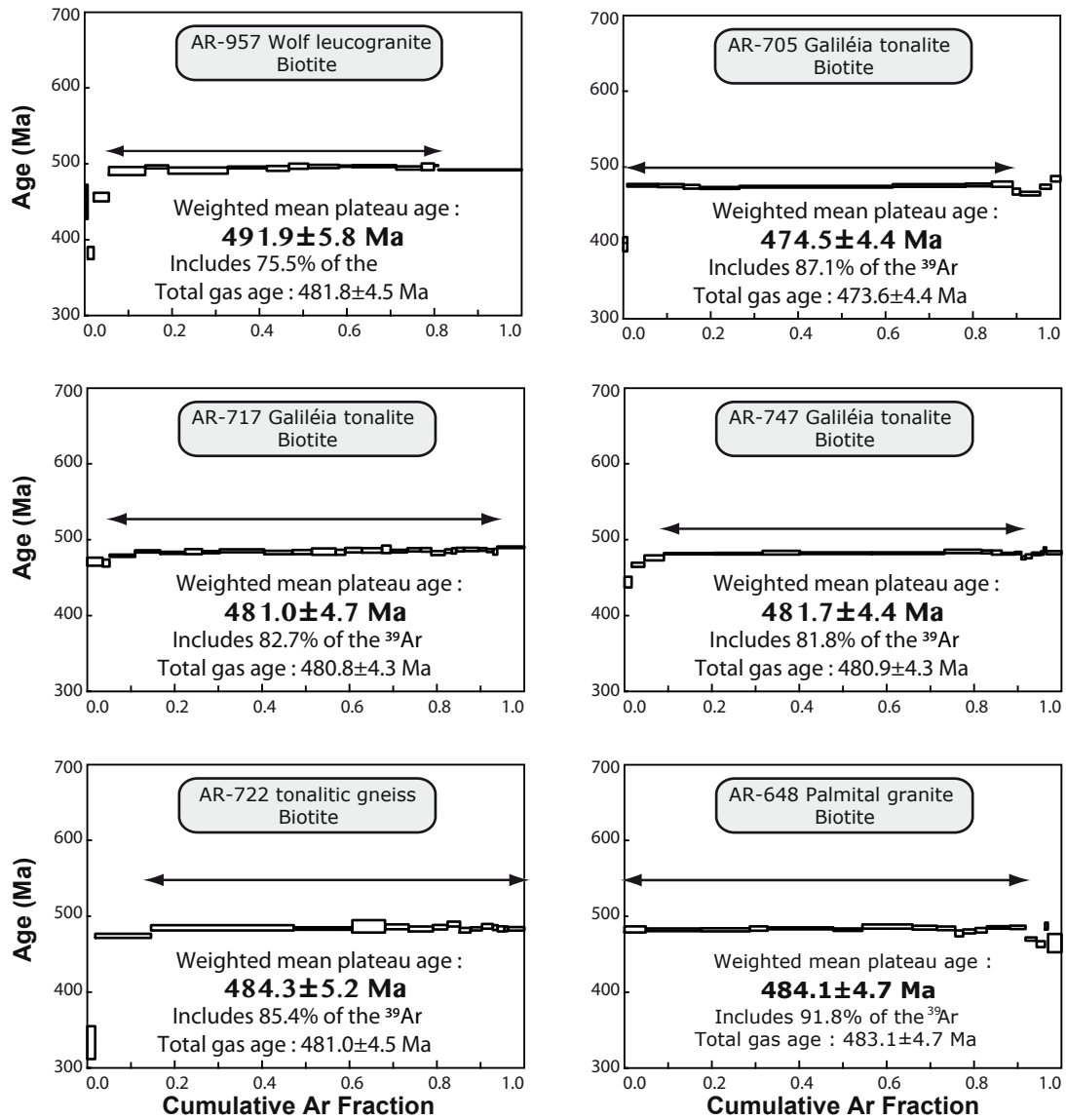


Figure 8:  $^{40}\text{Ar}/^{39}\text{Ar}$  diagrams for amphibole, muscovite and biotite from samples collected in the Central Plutonic Unit. Diagrams are organized by mineral and for samples from West to East. Analytical data and methodology are available in supplementary material #3.



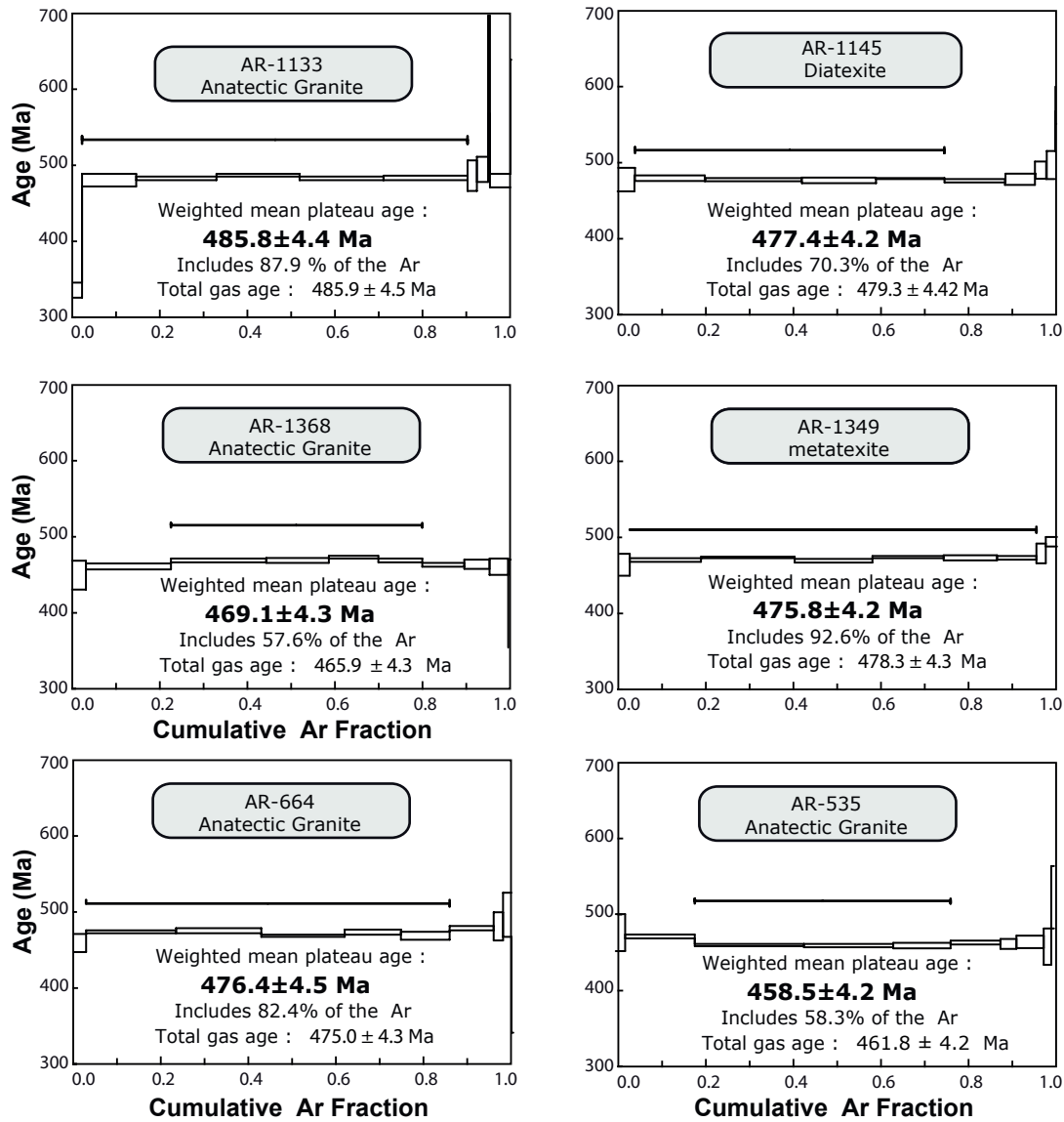


Figure 9:  $^{40}\text{Ar}/^{39}\text{Ar}$  diagrams for biotite from samples collected in the Eastern Anatectic Unit. Diagrams are displayed for samples from North to South. Analytical data and methodology are available in supplementary data #4.

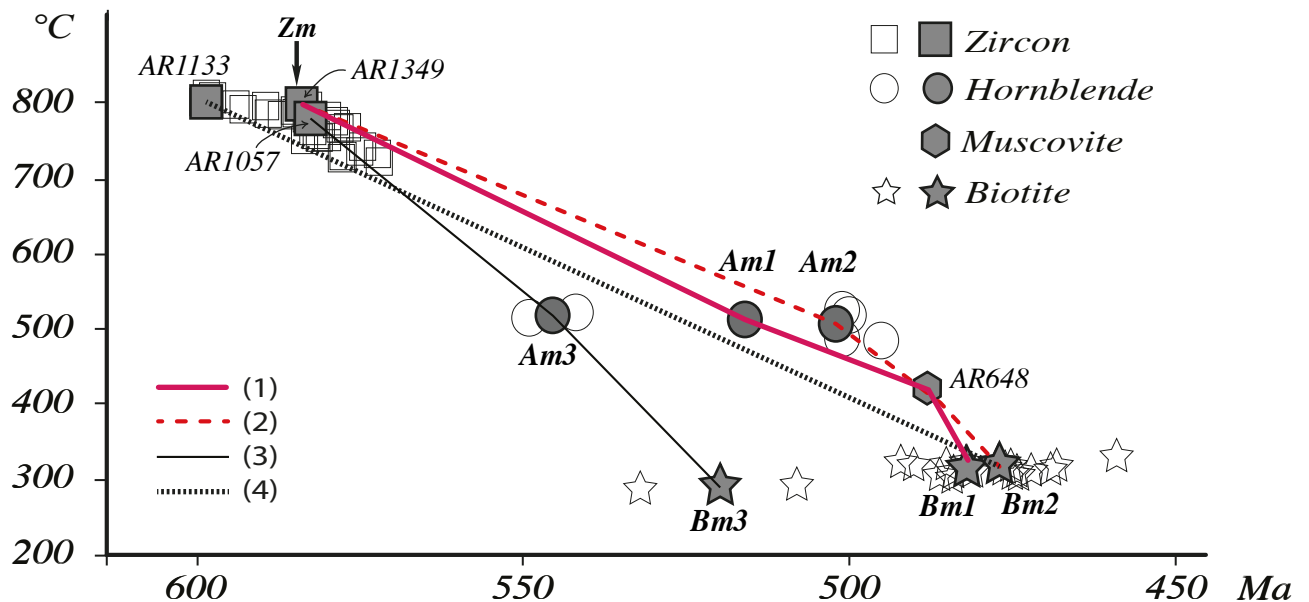


Figure 10: Diagram summarizing data and inferred thermochronological evolutions for the studied domain of the Araçuaí belt. Open symbols represents the whole set of data taken into account in this study. Symbols filled in grey represent either data for specific samples (zircons, muscovite) or average values computed for amphibole and biotite. Temperatures for zircons data have been roughly estimated from (a) the peak temperature (800 °C) and the oldest age (597 Ma) of the Eastern Anatectic Unit, (b) The Zn-in rutile temperature (780-790 °C) obtained for sample AR-1349 (583 Ma), (c) equilibrium temperatures (~750 °C) and ages (577-578 Ma) obtained for samples from the Western Mylonitic Unit, and (d) Ti-in-zircon temperature obtained for several samples from the EAU. Zm is average U-Pb age of zircons from synkinematic magmatic/anatectic rocks, Am are average  $^{40}\text{Ar}/^{39}\text{Ar}$  ages of amphiboles with Am1 for all dated samples and Am2 and Am3 without and for the two oldest samples, respectively. Similarly, Bm are average  $^{40}\text{Ar}/^{39}\text{Ar}$  ages of biotites with Bm1 for all dated samples and Bm2 and Bm3 without and for the two oldest samples, respectively. Line (1) represents the thermochronological evolution based on average values for all dated samples, (2) excludes the two oldest amphiboles and biotites, (3) is the cooling evolution based on the mean ages of the two oldest amphiboles and biotites, and (4) links the oldest zircons ages of the Eastern Anatectic unit to average age of biotites.

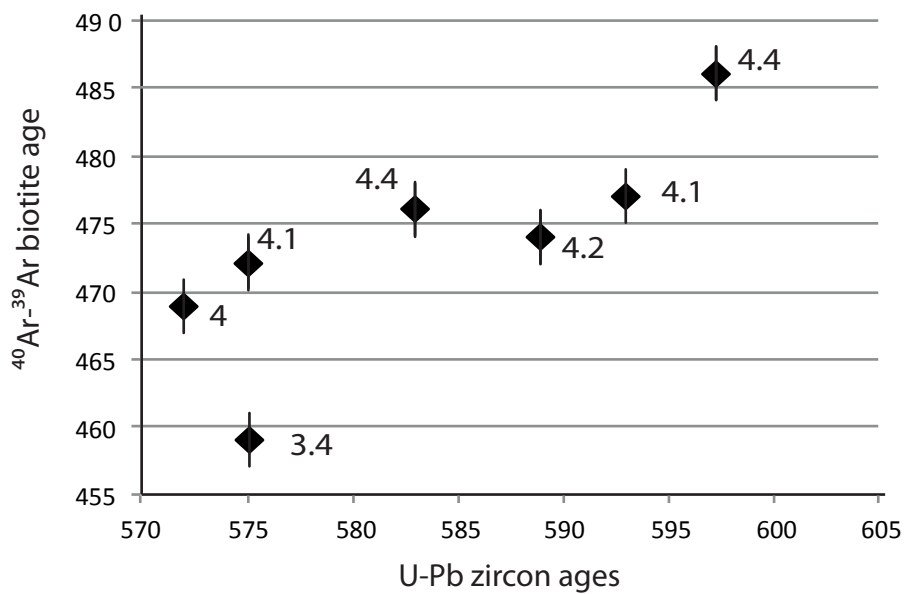


Figure 11: U-Pb zircon ages versus  $^{40}\text{Ar}/^{39}\text{Ar}$  biotite ages in the Eastern Anatectic Unit. Numbers are for the cooling rate calculated for each sample (Table 1). This figure shows a tendency of the age of closure of the  $^{40}\text{Ar}/^{39}\text{Ar}$  system in biotite to be correlated with zircon crystallization ages. Samples showing earlier crystallization of zircon also show earlier closure of the Ar/Ar system in biotite. This suggests a diachronous thermal evolution across the EAU.

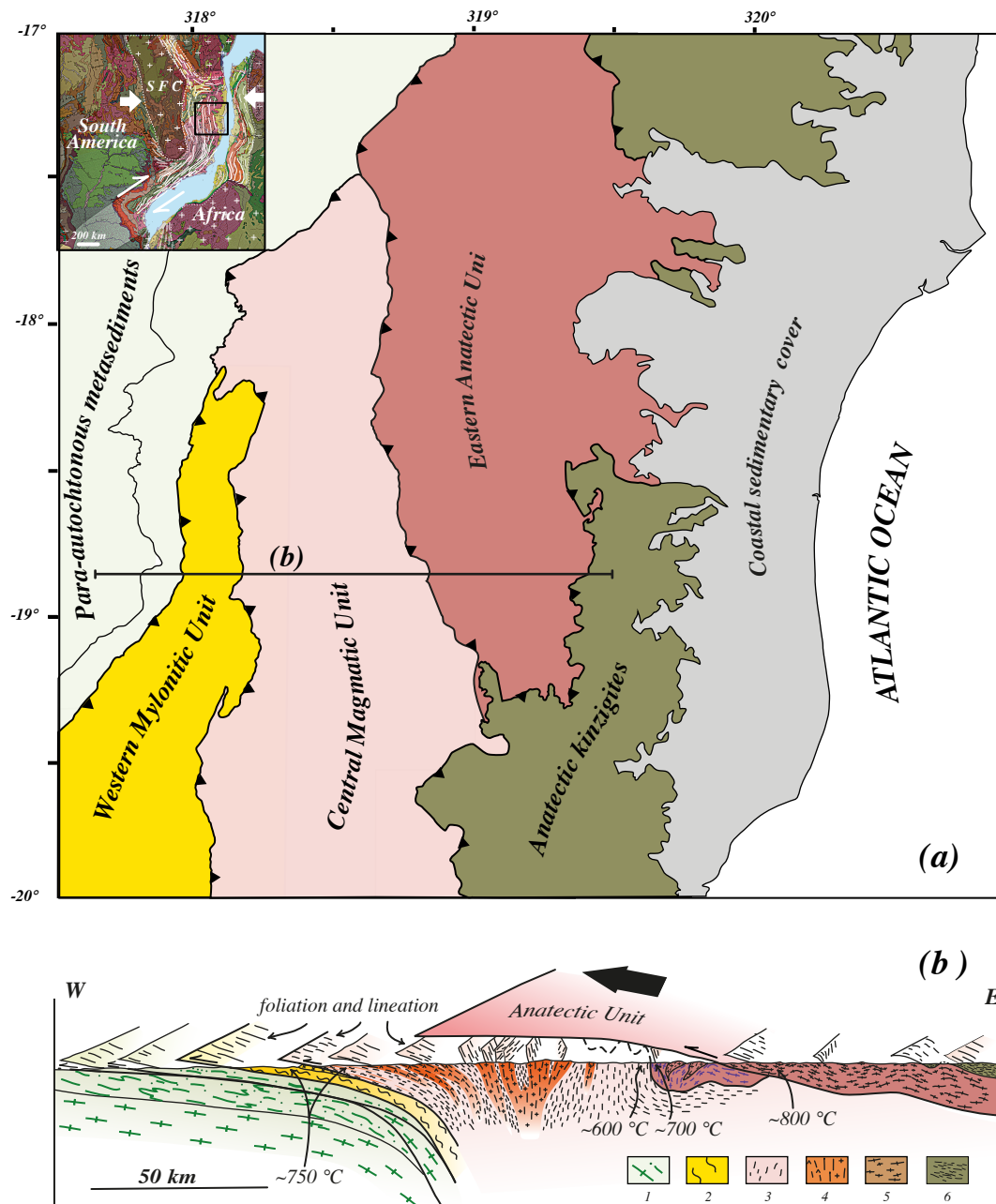
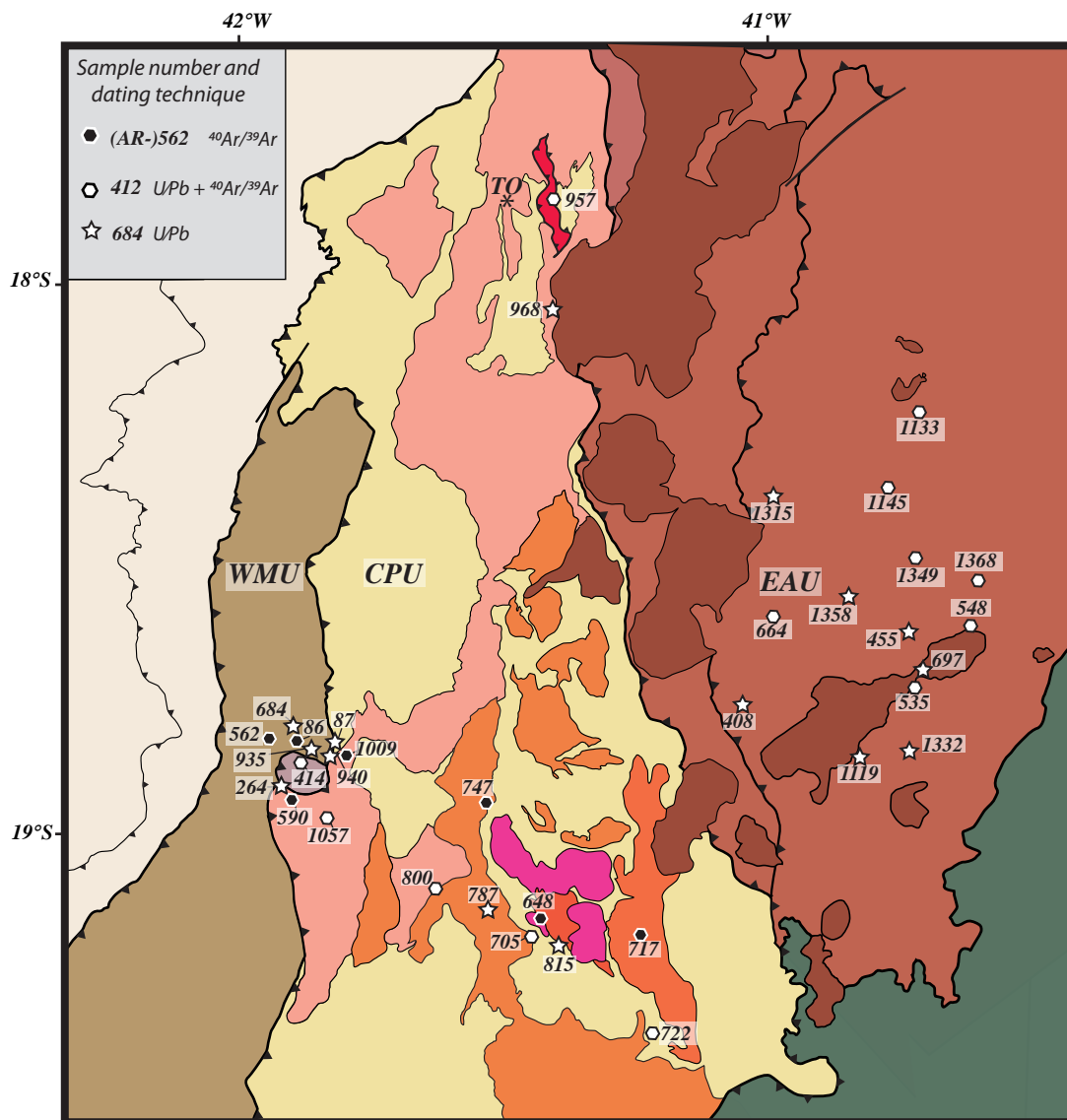


Figure 12: Schematic map and cross-section showing the Eastern Anatectic Unit thrust upon the Central and Western Units and even, in the northernmost part of the map, directly onto the para-autochthonous metasedimentary cover of the São Francisco craton. The cross-section also shows that the gently dipping basal contact of the Eastern unit crosscuts steeply dipping tectonic contacts and foliation in the eastern part of the CPU, suggesting that the tectonic emplacement of the EAU is later than the formation of this subvertical fabric, although it occurred before the anatexites reached solid-state.



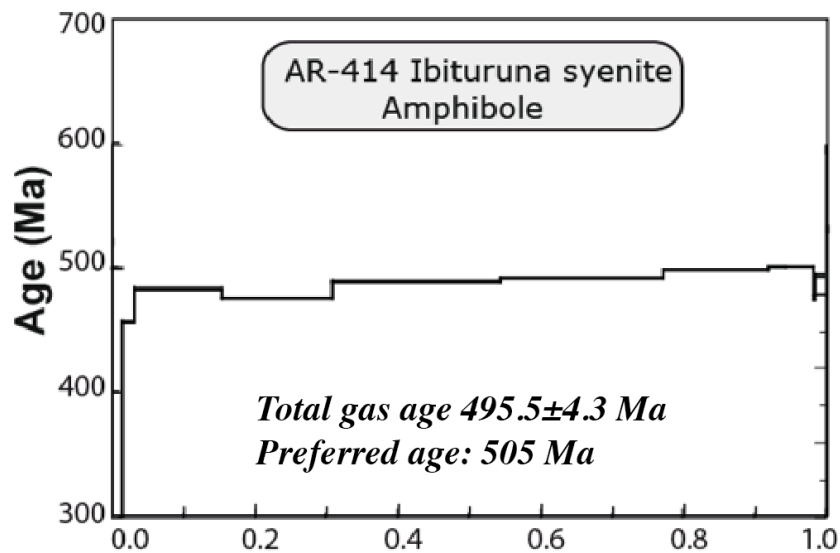
Supplementary material #1: Location of samples from which zircons and/or amphibole, biotite and muscovite have been dated. Results (and references for data already published) are summarized in Table 1, Figure 4 for zircons and Figure 7 for  $^{40}\text{Ar}/^{39}\text{Ar}$  ages. In the main text, sample numbers are preceded by AR- (for instance 562 is AR-562). Legends of the map as in Figure 2.

Supplementary material #2:

***<sup>40</sup>Ar/<sup>39</sup>Ar data and diagram for sample AR-414 (Petitgirard et al., 2009).***

Amphibole from this sample (Ibituruna syenite) did not yield a plateau age but a total gas age of  $495.4 \pm 4.3$  Ma that should be considered as a minimum age for its closure for argon. Apparent ages slightly increase with increasing degassing temperatures up to apparent ages in the range 500-510 Ma corresponding to almost constant  $^{37}\text{Ar}/^{39}\text{Ar}$  (Ca/K) and  $^{38}\text{Ar}/^{39}\text{Ar}$  (Cl/K) compositions. We thus preferred taking into account the integrated age of  $505 \pm 5$  Ma for the amphibole from this sample.

<i>AR414 Ibituruna Syenite Amphibole</i>					<i>Data from Petitgirard et al., 2009</i>				
Step	<sup>40</sup> Ar/ <sup>39</sup> Ar	<sup>38</sup> Ar/ <sup>39</sup> Ar	<sup>37</sup> Ar/ <sup>39</sup> Ar	<sup>36</sup> Ar/ <sup>39</sup> Ar (E-3)	F <sup>39</sup> Ar released	% <sup>40</sup> Ar*	<sup>40</sup> */ <sup>39</sup> Ar <sub>K</sub>	Age (Ma)	±1 SD (Ma)
1	51.133	0.085	0.2841	133.399	0.99	22.90	11.71	186.1	2.2
2	44.631	0.074	0.1807	93.225	1.49	38.26	17.08	265.4	2.2
3	41.129	0.048	0.0574	30.448	3.08	78.08	32.12	470.5	0.6
4	34.864	0.040	0.0072	3.000	15.41	97.40	33.96	494.1	0.2
5	33.716	0.053	0.1632	0.863	30.92	99.21	33.45	487.6	0.3
6	34.722	0.115	0.9239	1.309	54.47	98.99	34.39	499.6	0.4
7	34.715	0.189	1.8392	0.875	77.15	99.52	34.59	502.1	0.2
8	35.299	0.218	2.2291	1.184	91.93	99.33	35.11	508.7	0.2
9	35.967	0.224	2.5280	3.007	94.47	97.90	35.27	510.7	0.4
10	35.832	0.247	2.7335	2.467	98.33	98.37	35.31	511.2	0.3
11	37.297	0.250	2.6180	13.641	98.63	89.56	33.46	487.7	1.7
12	41.118	0.249	2.6689	22.207	100.00	84.38	34.76	504.3	1.1



Petitgirard, S., Vauchez, A., Egydio-Silva, M., Bruguier, O., Camps, P., Monié, P., Babinski, M. and Mondou, M., 2009. Conflicting structural and geochronological data from the Ibituruna quartz-syenite (SE Brazil): Effect of protracted "hot" orogeny and slow cooling rate? *Tectonophysics* 477, 174-196.

Supplementary material #3:

*Ar- Ar results for samples from the Central Plutonic Unit*

**Method:**

These samples were collected for laser probe single grain  $^{40}\text{Ar}$ - $^{39}\text{Ar}$  studies at Geosciences Montpellier (Université de Montpellier, France). They were hand crushed and cleaned using ethanol and distilled water. Single grains of amphibole and mica about 500  $\mu\text{m}$  in diameter were handpicked under binocular microscope and ultrasonically cleaned in acetone and distilled water. The grains were then packaged in aluminium foils and irradiated along with several flux monitors of MMhb-1 hornblende and TCR2-sanidine at McMaster Reactor (Canada) with an integrated power of 60 MWH.  $\text{K}_2\text{SO}_4$  and  $\text{CaF}_2$  salts were also irradiated to determine the correction factors for interference reactions from K and Ca.  $^{40}\text{Ar}$ - $^{39}\text{Ar}$  laser degassing was carried out at Geosciences Montpellier (France) using a 50W  $\text{CO}_2$  laser. The gas cleaning was achieved in a low volume UHV gas purification system including a cold trap and two Ti/Zr getters. Argon isotope measurements were performed on a MAP215-50 noble gas mass spectrometer directly connected to the UHV purification system. Blank analyses were performed every three runs to eliminate the background contribution on the gas released from the sample itself. Individual grains were stepwise heated by increasing the laser beam intensity in successive increments until the final fusion. A plateau age is defined by three or more contiguous heating steps comprising 50% or more of the  $^{39}\text{Ar}_\text{K}$  released and overlapping at the two-sigma confidence level. Because of the high radiogenic content of the dated minerals and the clustering of data points near the  $^{39}\text{Ar}$ - $^{40}\text{Ar}$  abscissa,  $^{36}\text{Ar}$ - $^{40}\text{Ar}$  versus  $^{39}\text{Ar}$ - $^{40}\text{Ar}$  correlation plots do not provide meaningful information about the age and initial  $^{36}\text{Ar}$ - $^{40}\text{Ar}$  values.

**Results:**

Step	$^{40}\text{Ar}/^{39}\text{Ar}$	$^{38}\text{Ar}/^{39}\text{Ar}$	$^{37}\text{Ar}/^{39}\text{Ar}$	$^{36}\text{Ar}/^{39}\text{Ar}$ (E-3)	F $^{39}\text{Ar}$ released	% $^{40}\text{Ar}^*$	$^{40*}/^{39}\text{Ar}_\text{K}$	Age (Ma)	$\pm 1$ SD (Ma)
<i>AR-590 Derribadinha tonalite Amphibole</i>									
1	1190.597	0.088	0.00163	115.344	0.01	97.14	1156.5	4440.84	959.0
2	525.881	0.414	37.06841	395.543	0.05	78.30	421.95	2871.623	139.9
3	40.087	0.055	0.07051	11.151	12.52	91.75	36.78	529.416	2.8
4	38.401	0.053	0.00000	3.618	16.75	97.17	37.32	536.056	3.8
5	38.749	0.053	0.00000	3.893	23.39	96.99	37.58	539.361	2.4
6	37.889	0.054	0.00000	1.733	36.33	98.61	37.36	536.607	1.5
7	38.485	0.05	0.00000	2.784	39.29	97.82	37.65	540.157	2.3
8	39.338	0.052	0.88118	4.345	41.82	96.86	38.13	546.099	2.4
9	40.045	0.053	0.22236	5.34	45.71	96.06	38.47	550.377	3.4
10	38.602	0.197	9.80187	4.637	58.67	98.32	38.2	546.953	1.8
11	38.792	0.22	8.05135	4.118	66.52	98.38	38.36	549.036	2.3
12	38.736	0.234	8.42765	3.584	89.15	98.86	38.5	550.762	1.2
13	37.921	0.149	4.41234	3.567	92.30	98.05	37.29	535.727	3.7

14	38.258	0.119	3.12708	2.99	100.00	98.26	37.67	540.452	2.3
<b>AR-590 Derribadinha tonalite Biotite</b>									
1	260.267	0.279	0.85808	821.286	0.12	6.77	17.64	273.22	249.9
2	47.308	0.078	0.30582	47.638	0.99	70.26	33.24	484.733	8.4
3	37.783	0.055	0.00454	4.487	9.95	96.45	36.44	525.151	1.9
4	38.096	0.056	0.02386	5.614	14.51	95.61	36.42	524.927	2.4
5	37.547	0.054	0.00000	1.838	23.02	98.51	36.99	531.976	1.9
6	36.978	0.051	0.00894	0.905	30.26	99.24	36.70	528.325	2.8
7	37.316	0.052	0.00000	1.352	39.65	98.89	36.90	530.883	1.5
8	37.577	0.052	0.02104	1.507	44.11	98.78	37.12	533.591	2.0
9	37.213	0.052	0.00000	1.592	50.89	98.69	36.73	528.715	2.5
10	37.553	0.053	0.01094	1.671	54.61	98.65	37.04	532.675	2.6
11	37.395	0.054	0.00957	1.835	58.77	98.51	36.84	530.104	2.1
12	37.339	0.054	0.00419	1.298	71.42	98.93	36.94	531.374	1.7
13	38.200	0.054	0.02762	2.665	77.27	97.90	37.40	537.086	2.2
14	37.479	0.053	0.00051	1.614	82.08	98.69	36.99	531.947	1.5
15	37.740	0.053	0.00000	1.817	87.03	98.54	37.19	534.458	2.2
16	37.682	0.054	0.01606	1.812	93.55	98.54	37.13	533.775	1.7
17	37.827	0.052	0.00000	2.458	100.00	98.04	37.09	533.182	2.3
<b>AR-1057 São Vitor tonalite Amphibole</b>				J= 0.009621					
1	1318.154	5.167	0.01591	4055.33	0.01	9.09	119.79	1383.1	7131.5
2	137.46	1.089	0.00341	248.554	0.06	46.56	64	865.6	1790.6
3	87.653	1.146	0.00438	857.07	0.10	-188.96	-165.63	0.0	0.0
4	73.132	0.824	0.00216	49.913	0.19	79.81	58.37	804.0	1148.4
5	26.992	0.121	0.00062	0.002	0.47	99.94	26.98	416.3	14.2
6	33.716	0.136	0.00121	0.003	0.62	99.95	33.7	506.6	23.1
7	33.403	0	0.00064	0.002	0.90	99.95	33.39	502.5	11.7
8	36.065	0.038	0.00015	0	2.13	99.96	36.05	537.2	6.9
9	36.223	0.103	0.00001	0	24.26	99.96	36.21	539.2	8.1
10	36.476	0.083	0.00003	0	29.92	99.96	36.46	542.5	4.1
11	36.61	0.11	0.00000	0	67.39	99.96	36.59	544.2	7.7
12	36.231	0.073	0.00003	0	74.18	99.96	36.22	539.3	10.1
13	36.788	0.053	0.00014	0	75.42	99.96	36.77	546.5	8.0
14	36.393	0.09	0.00003	0	82.57	99.96	36.38	541.4	2.8
15	36.267	0.055	0.00001	0	100.00	99.96	36.25	539.8	6.7
<b>AR-1057 São Vitor tonalite Biotite</b>				J= 0.009621					
1	110.008	0.856	51.77421	633.621	0.02	-66.68	-75.92	0.0	0.0
2	55.347	0.118	42.76951	156.805	0.05	22.05	12.55	205.7	635.9
3	19.962	0	27.29096	4.961	0.12	99.92	20.9	330.5	253.3
4	30.371	0.041	1.20390	11.343	0.44	89.21	27.12	418.2	54.5
5	32.03	0.03	0.00003	2.986	1.30	97.2	31.13	472.7	20.0
6	34.103	0.024	5.91843	19.592	2.40	84.28	28.85	442.0	16.0
7	33.375	0.021	0.00001	0	5.04	99.95	33.36	502.2	4.0
8	33.621	0.021	0.00001	0	7.65	99.95	33.61	505.4	2.4
9	33.872	0.022	0.00001	0.173	10.01	99.8	33.81	508.0	8.0
10	33.672	0.019	0.00001	0	14.42	99.95	33.66	506.1	2.1
11	33.639	0.017	0.00001	0	18.01	99.95	33.62	505.6	4.1
12	33.621	0.013	0.00001	0	20.48	99.95	33.61	505.4	4.8
13	33.401	0.025	0.68492	0	25.61	99.95	33.45	503.4	3.8
14	33.81	0.019	0.00001	0	29.71	99.95	33.79	507.9	2.6



15	33.405	0.016	0.15295	0	33.97	99.95	33.4	502.8	3.5
16	33.596	0.018	0.00995	0	36.51	99.95	33.58	505.1	1.9
17	33.77	0.019	0.47576	0	39.37	99.95	33.8	508.0	1.9
18	33.827	0.028	0.09567	0	48.56	99.95	33.82	508.2	5.0
19	33.52	0.018	0.00001	0	53.17	99.95	33.5	504.1	3.1
20	33.961	0.019	0.00000	0	61.48	99.95	33.95	509.9	2.6
21	33.56	0.021	0.00001	0.725	64.49	99.32	33.33	501.8	5.9
22	33.94	0.021	0.00001	0	68.98	99.95	33.92	509.6	2.6
23	33.895	0.019	0.00001	0	72.19	99.95	33.88	509.0	4.8
24	33.485	0.021	0.39021	0	78.31	99.95	33.51	504.1	8.5
25	33.807	0.018	0.03891	0.776	81.48	99.28	33.57	504.9	6.2
26	33.809	0.02	0.11646	0.905	85.65	99.19	33.54	504.5	4.8
27	33.911	0.02	0.00000	0	92.58	99.95	33.9	509.2	1.4
28	33.821	0.019	0.00001	0	94.72	99.95	33.81	508.0	3.3
29	33.943	0.02	0.00001	0.354	98.05	99.65	33.82	508.2	5.8
30	33.419	0.023	0.00001	0	100.00	99.95	33.4	502.8	1.4
<b>AR-1009 São Vitor tonalite Amphibole</b> J= 0.009621									
1	240.903	2.011	0.00999	0.029	0.02	99.99	240.88	2163.5	187.3
2	110.055	0	0.00470	0.014	0.07	99.98	110.04	1302.6	104.3
3	31.356	0.142	0.00148	0.004	0.21	99.95	31.34	475.4	36.4
4	26.766	0	0.00195	0.006	0.31	99.94	26.75	413.1	43.5
5	13.629	0.094	0.00048	0.001	0.75	99.88	13.61	222.0	12.5
6	32.837	0.098	0.00007	0	3.84	99.95	32.82	495.1	5.7
7	32.942	0.092	0.00001	0	30.41	99.95	32.93	496.5	21.6
8	33.752	0.116	0.00001	0	56.55	99.95	33.74	507.1	10.3
9	33.243	0.104	0.00002	0	69.92	99.95	33.23	500.4	4.6
10	33.177	0.094	0.00001	0	89.86	99.95	33.16	499.6	7.7
11	36.04	0.126	0.00008	8.32	92.38	93.13	33.57	504.9	54.6
12	35.724	0.111	0.00749	9.601	100.00	92.02	32.87	495.7	19.3
<b>AR-1009 São Vitor tonalite Biotite</b> J= 0.009621									
1	17.141	0.063	0.00031	48.478	0.21	16.34	2.8	48.0	246.5
2	19.604	0.054	2.54802	27.182	0.64	59.92	11.77	193.5	112.0
3	30.648	0.027	0.23931	2.129	12.46	97.96	30.03	457.8	4.8
4	33.241	0.033	0.56846	3.592	21.69	96.89	32.22	487.1	5.9
5	32.232	0.025	0.00002	0	26.50	99.95	32.22	487.1	2.4
6	32.84	0.028	0.48662	3.662	34.88	96.77	31.79	481.4	6.6
7	32.752	0.028	0.70427	3.193	43.07	97.23	31.86	482.4	6.6
8	32.715	0.028	0.20325	0.356	64.36	99.68	32.61	492.3	3.6
9	32.546	0.023	0.00001	0	69.86	99.95	32.53	491.2	1.3
10	32.668	0.024	0.08151	0.609	82.04	99.42	32.48	490.6	4.4
11	32.741	0.018	1.23529	1.025	84.66	99.31	32.54	491.4	20.1
12	32.509	0.025	0.40070	1.045	100.00	99.09	32.22	487.2	2.5
<b>AR-800 São Vitor tonalite Biotite</b> J= 0.009621									
1	24.463	0.038	0.00042	0.001	0.24	99.93	24.45	381.1	11.0
2	27.11	0	0.00006	0	1.91	99.94	27.09	417.9	2.6
3	31.993	0.013	0.00000	0	24.01	99.95	31.98	483.9	3.2
4	32.104	0.01	0.03448	0	40.98	99.95	32.09	485.4	1.0
5	31.991	0.01	0.32973	0.101	65.29	99.94	31.98	483.9	2.8
6	31.174	0.01	1.67359	0.53	73.66	99.85	31.16	473.1	7.9
7	32.499	0.014	0.30455	1.315	87.06	98.83	32.12	485.9	4.3
8	31.573	0.015	0.92221	1.489	91.94	98.78	31.21	473.6	11.6
9	31.366	0.014	2.65175	0	96.19	99.95	31.6	479.0	2.1
10	29.342	0.012	5.49134	0	97.99	99.95	29.85	455.4	4.7

11	29.15	0.004	5.97273	0	100.00	99.95	29.7	453.4	2.3
<b>AR-705 Galiléia tonalite Biotite</b> J= 0.009143									
1	47.49	0.035	0.09484	69.249	0.96	56.89	27.02	398.3	9.4
2	34.542	0.019	0.04145	5.079	7.90	95.62	33.03	476.1	1.7
3	34.124	0.019	0.03185	3.779	13.88	96.69	32.99	475.6	2.0
4	34.076	0.018	0.02898	4.019	17.51	96.48	32.88	474.1	2.4
5	35.064	0.017	0.00153	7.771	26.51	93.41	32.75	472.6	1.3
6	33.221	0.017	0.00252	1.093	61.59	98.98	32.88	474.2	1.1
7	33.451	0.016	0.00933	1.446	78.28	98.68	33.01	475.8	1.7
8	33.74	0.015	0.00433	2.203	84.24	98.03	33.07	476.6	1.8
9	33.62	0.015	0.04585	1.566	89.05	98.59	33.15	477.6	3.5
10	33.468	0.019	0.00000	3.643	90.78	96.74	32.38	467.8	3.9
11	33.088	0.016	0.00000	3.046	95.39	97.23	32.17	465.2	2.4
12	33.857	0.021	0.01916	3.274	97.83	97.1	32.88	474.1	2.7
13	34.062	0.022	0.30465	1.224	100.00	98.96	33.71	484.7	3.7
<b>AR-957 Galiléia tonalite Biotite</b> J= 0.009621									
1	90.921	0.123	0.00007	220.372	0.47	28.36	25.79	399.8	45.0
2	28.051	0.133	0.00002	38.963	1.93	58.9	16.52	266.1	16.0
3	26.711	0.083	0.00001	0	5.44	99.94	26.7	412.4	11.3
4	31.753	0.099	0.00000	0	13.66	99.95	31.74	480.7	10.7
5	32.575	0.081	0.00001	0	19.06	99.95	32.56	491.6	4.1
6	31.829	0.095	0.00000	0	32.63	99.95	31.81	481.7	8.0
7	32.456	0.095	0.00000	0	41.55	99.95	32.44	490.1	2.4
8	32.39	0.087	0.74200	0.619	46.68	99.56	32.26	487.7	6.4
9	32.439	0.088	2.72211	0	51.05	99.95	32.69	493.3	6.8
10	32.654	0.063	0.00000	0	58.09	99.95	32.64	492.7	4.2
11	32.703	0.104	0.19190	0	61.17	99.95	32.71	493.6	1.7
12	32.701	0.069	0.00000	0	71.31	99.95	32.69	493.3	2.6
13	32.35	0.1	0.00001	0	77.13	99.95	32.33	488.7	4.4
14	32.634	0.087	1.00316	0.444	79.83	99.78	32.58	491.9	8.7
15	32.839	0.062	0.00003	0	80.90	99.95	32.82	495.1	1.0
16	31.988	0.12	0.18118	0	100.00	99.95	31.99	484.1	1.0
<b>AR-747 Galiléia tonalite Biotite</b> J= 0.009143									
1	57.422	0.03	0.01364	91.03	1.61	53.13	30.51	443.9	7.1
2	39.955	0.022	0.02162	25.911	4.52	80.8	32.28	466.6	2.8
3	35.88	0.016	0.00738	9.687	9.02	91.98	33	475.7	3.3
4	34.273	0.015	0.00168	2.766	20.32	97.57	33.44	481.3	0.9
5	34.296	0.015	0.00014	2.832	31.62	97.51	33.44	481.3	1.1
6	33.764	0.015	0.01223	0.697	40.13	99.35	33.54	482.6	2.4
7	33.859	0.015	0.00433	1.196	56.64	98.91	33.49	481.9	1.1
8	33.859	0.015	0.00036	1.196	73.15	98.91	33.49	481.9	1.1
9	34.115	0.015	0.00573	1.423	81.64	98.72	33.68	484.3	2.2
10	34.308	0.015	0.00025	2.258	84.00	98.01	33.63	483.6	1.9
11	33.948	0.016	0.00000	1.262	86.30	98.86	33.56	482.8	2.7
12	34.072	0.016	0.00000	2.071	89.38	98.16	33.44	481.3	1.2
13	34.353	0.016	0.00000	2.806	90.79	97.54	33.51	482.1	1.5
14	33.582	0.014	0.01767	1.878	91.79	98.31	33.01	475.9	2.1
15	33.964	0.016	0.09576	2.674	93.24	97.65	33.17	477.8	2.6
16	34.171	0.015	0.04058	2.497	95.25	97.8	33.42	481.0	1.7
17	34.185	0.013	0.03524	2.226	95.88	98.04	33.51	482.2	2.4
18	35.065	0.012	0.04808	3.948	96.45	96.64	33.89	486.9	2.7
19	34.571	0.016	0.37912	3.552	100.00	97	33.54	482.6	2.1

<i>AR-722 Orthogneiss Biotite</i>				J= 0.009143					
1	159.363	0.099	0.00000	464.193	1.87	13.92	22.18	333.1	21.7
2	34.741	0.014	0.00000	6.242	14.58	94.65	32.88	474.2	2.6
3	34.216	0.014	0.00000	1.643	47.17	98.54	33.72	484.7	3.5
4	33.938	0.014	0.01015	0.977	60.65	99.11	33.63	483.7	1.7
5	33.969	0.014	0.01127	0.317	68.16	99.68	33.86	486.6	8.2
6	34.18	0.013	0.00113	1.167	73.52	98.95	33.82	486.1	3.3
7	33.726	0.016	0.00313	0.389	79.06	99.61	33.6	483.3	3.3
8	33.956	0.014	0.00000	0.523	82.42	99.5	33.79	485.6	3.1
9	34.568	0.015	0.04584	1.497	85.25	98.68	34.11	489.8	3.2
10	34.858	0.01	0.04797	4.659	87.71	96.02	33.47	481.7	3.2
11	34.272	0.016	0.00315	2.179	90.25	98.08	33.61	483.5	2.2
12	34.487	0.01	0.00000	2.001	92.79	98.24	33.88	486.8	3.1
13	34.305	0.008	0.04174	1.852	93.90	98.37	33.75	485.1	3.2
14	33.628	0.013	0.00000	0	95.50	99.95	33.61	483.5	3.4
15	35.277	0.016	0.00000	5.575	96.17	95.29	33.61	483.5	3.1
16	33.888	0.015	0.00000	0.891	100.00	.18	33.61	483.4	2.4
<i>AR-717 Galiléia tonalite Amphibole</i>				J= 0.009143					
1	34.57	0.087	2.81088	1.655	9.34	99.15	34.34	492.6	1.7
2	35.003	0.1	3.03178	0.741	43.23	99.96	35.07	501.7	1.0
3	36.44	0.098	2.87131	5.795	46.51	95.85	34.99	500.8	1.9
4	34.743	0.099	3.01849	0.501	71.53	99.96	34.87	499.3	0.8
5	35.207	0.097	3.19382	1.54	74.55	99.34	35.05	501.5	3.4
6	34.857	0.094	3.17437	0.909	77.87	99.87	34.88	499.4	3.6
7	33.844	0.093	3.06684	1.285	81.76	99.51	33.75	485.1	1.4
8	34.243	0.096	3.08908	1.2	84.98	99.6	34.17	490.5	2.8
9	34.695	0.089	3.04323	0	86.34	99.96	34.98	500.6	2.8
10	34.46	0.087	3.50846	0	87.96	99.95	34.79	498.2	2.2
11	34.269	0.101	4.06140	0.423	89.99	99.95	34.52	494.9	3.4
12	34.294	0.086	4.88181	1.663	100.00	99.59	34.26	491.6	1.8
<i>AR-717 Galiléia tonalite Biotite</i>				J= 0.009143					
1	69.019	0.051	0.01228	123.733	3.52	47	32.44	468.6	4.8
2	41.894	0.034	0.00000	32.376	5.10	77.13	32.31	467.0	4.2
3	39.081	0.029	0.00000	20.501	10.99	84.46	33.01	475.8	1.4
4	37.388	0.03	0.00000	13.371	16.72	89.39	33.42	481.0	1.4
5	36.138	0.028	0.00294	9.623	22.38	92.09	33.28	479.2	1.3
6	36.239	0.027	0.00000	9.562	26.30	92.16	33.4	480.7	3.0
7	35.741	0.027	0.01162	8.044	30.38	93.31	33.35	480.1	1.3
8	34.784	0.027	0.00000	4.364	40.46	96.25	33.48	481.8	1.8
9	34.724	0.026	0.00451	4.722	46.91	95.94	33.31	479.7	2.1
10	34.831	0.024	0.00000	4.944	51.38	95.76	33.35	480.2	2.5
11	34.462	0.026	0.00000	3.546	56.80	96.91	33.4	480.8	3.9
12	34.525	0.025	0.01044	3.976	59.00	96.55	33.34	480.0	3.0
13	34.477	0.025	0.00000	3.118	62.83	97.28	33.54	482.5	2.7
14	34.058	0.027	0.00000	1.788	67.39	98.4	33.51	482.2	2.7
15	34.103	0.028	0.00000	1.581	69.44	98.58	33.62	483.6	4.6
16	33.701	0.026	0.00000	0.809	73.23	99.24	33.45	481.4	1.6
17	33.807	0.026	0.00000	0.726	76.31	99.32	33.58	483.0	2.0
18	34.128	0.026	0.00000	1.843	78.69	98.36	33.57	482.9	2.2
19	33.742	0.023	0.00778	1.58	81.84	98.57	33.26	479.0	2.4
20	33.921	0.026	0.05392	1.562	83.39	98.6	33.45	481.4	2.1
21	34.031	0.026	0.13242	1.878	84.41	98.35	33.47	481.7	3.2
22	34.255	0.027	0.07780	2.209	86.16	98.07	33.59	483.2	2.2
23	34.088	0.025	0.00000	1.579	89.48	98.59	33.61	483.4	2.0

24	34.182	0.023	0.00000	1.897	91.45	98.31	33.61	483.4	1.7
25	34.433	0.026	0.00000	3.116	92.87	97.28	33.5	482.0	1.8
26	34.898	0.026	0.06806	5.072	93.74	95.68	33.39	480.7	3.5
27	34.888	0.026	0.07908	3.617	100.00	96.91	33.81	486.0	1.0
<b>AR-648 Palmital granite Muscovite</b> <div>J=0.009143</div>									
1	44.588	0.045	0.00000	33.342	0.32	77.87	34.72	497.4	15.8
2	41.464	0.014	0.08912	25.844	1.44	81.56	33.82	486.1	4.0
3	34.49	0.012	0.00096	1.894	38.29	98.33	33.91	487.3	0.9
4	34.152	0.011	0.00000	0.74	63.38	99.31	33.92	487.3	2.3
5	34.333	0.013	0.03045	1.628	67.35	98.56	33.84	486.3	3.7
6	34.304	0.015	0.00066	1.067	71.51	99.04	33.97	488.0	1.9
7	34.057	0.011	0.00000	0	79.71	99.95	34.04	488.9	2.2
8	34.116	0.012	0.01782	0.308	87.49	99.69	34.01	488.5	1.2
9	33.864	0.011	0.04417	0.046	88.52	99.92	33.84	486.3	3.3
10	34.07	0.012	0.00000	0.058	94.25	99.9	34.04	488.8	0.9
11	33.329	0.009	0.01615	0	96.75	99.95	33.31	479.7	1.4
12	34.258	0.011	0.00364	0	99.74	99.95	34.24	491.4	1.5
13	34.001	0.014	0.00000	0	100.00	99.95	33.99	488.2	11.5
<b>AR-648 Palmital granite Biotite</b> <div>J= 0.009143</div>									
1	52.46	0.026	0.00710	63.792	4.90	64.04	33.59	483.2	3.9
2	40.419	0.018	0.00657	23.181	17.64	83.02	33.55	482.7	1.7
3	37.645	0.017	0.00113	13.793	28.62	89.13	33.55	482.7	2.0
4	38.948	0.016	0.00414	17.756	32.78	86.49	33.69	484.4	2.8
5	36.093	0.017	0.00274	8.039	47.76	93.38	33.7	484.6	1.3
6	35.885	0.014	0.02312	7.814	54.41	93.53	33.56	482.8	1.6
7	35.43	0.015	0.00000	5.172	65.86	95.64	33.89	486.9	2.7
8	35.595	0.015	0.00000	6.099	71.54	94.89	33.78	485.5	2.5
9	35.949	0.014	0.02017	7.55	75.61	93.75	33.7	484.6	2.4
10	35.756	0.013	0.07064	8.661	77.47	92.81	33.19	478.1	3.8
11	35.479	0.016	0.02246	7.019	80.25	94.11	33.39	480.7	2.5
12	35.548	0.015	0.00000	6.866	82.88	94.25	33.5	482.1	2.9
13	35.359	0.016	0.00000	5.228	88.15	95.59	33.8	485.8	1.6
14	35.204	0.015	0.01110	4.678	91.77	96.03	33.81	485.9	2.2
15	32.629	0.012	0.01785	0	94.27	99.95	32.62	470.8	2.1
16	32.112	0.014	0.03756	0	96.17	99.95	32.1	464.3	3.8
17	36.991	0.015	0.00000	10.295	96.92	91.73	33.93	487.5	4.5
18	126.985	0.072	0.00000	320.696	100.00	25.36	32.2	465.6	11.8

*Ar- Ar results for samples from the Eastern Anatectic Unit***Method:**

Samples from the Eastern Anatectic Unit were processed and analysed at the Geochronological Research Center of the University of São Paulo (Brazil). Separation and concentration consisted of hand crushing of centimetre-scale sample chips using steel pestle and mortar to reduce size to mm-scale, sieving for size fractions of #250-500, and final magnetic purification through a isodynamic Frantz® separator. Biotite was loaded into a 21-pit aluminum disk along with the Fish Canyon sanidine standard (FCs) arranged in a cross-like geometry. Neutron-flux irradiation was performed in the cadmium lined in-core (CLICIT) facility at the Oregon State University TRIGA reactor for 14 hours. After radioactive cooling (approximately 4 weeks), each sample was loaded on a Cu-disk as multigrain aliquots containing two or three irradiated biotite flakes and progressively step-heated by a solid state Nd:YVO<sub>4</sub> (532 nm) Verdi 6W Coherent laser. Data reduction including correction for nuclear interferences, background (blank) and mass discrimination, as well J-value determination and graphical representation were made using the Ar-ArCALC v2.5.2 software (Koppers, 2012). The ages were calculated relative to the age of  $28.01 \pm 0.04$  Ma for the FCs standard (Phillips and Matchan, 2013a; Phillips and Matchan, 2013b), assuming the <sup>40</sup>K decay constant of Steiger and Jäger (Steiger and Jäger, 1977). The J-factor value for this irradiation is  $0.00406 \pm 0.00002$ .

**Results:**

Step	<sup>39</sup> Ar released %	<sup>40</sup> Ar/ <sup>39</sup> Ar	1σ	<sup>37</sup> Ar/ <sup>39</sup> Ar	1σ	<sup>36</sup> Ar/ <sup>39</sup> Ar	1σ	<sup>39</sup> Ar <sub>K</sub> (%)	<sup>40</sup> Ar*(%)	<sup>40</sup> Ar*/ <sup>39</sup> Ar <sub>K</sub>	2σ	Age (Ma)	2σ
<b>AR-535 Anatectic granite biotite</b>													
1	2.1	75.104	0.426	0.0949	0.0321	0.0037	0.0071	2.09	98.53	74.00	4.30	475.06	24.30
2	18.0	72.939	0.018	0.0183	0.0059	-0.0006	0.0007	15.81	100.23	73.11	0.45	470.01	2.54
3	42.8	71.218	0.091	0.0171	0.0022	0.0003	0.0003	24.87	99.88	71.13	0.26	458.80	1.49
4	63.1	71.345	0.044	0.0118	0.0033	0.0012	0.0006	20.45	99.50	70.99	0.39	457.97	2.23
5	76.3	71.988	0.118	0.0203	0.0057	0.0033	0.0010	13.12	98.65	71.02	0.64	458.14	3.67
6	87.6	71.965	0.087	0.0785	0.0042	0.0008	0.0007	11.28	99.70	71.75	0.48	462.30	2.72
7	91.2	73.069	0.295	-0.1005	0.0072	0.0055	0.0016	3.70	97.75	71.42	1.11	460.44	6.30
8	97.5	72.664	0.144	-0.0329	0.0081	0.0027	0.0023	6.25	98.90	71.86	1.40	462.94	7.98
9	99.1	75.197	0.942	-0.0306	0.0213	0.0148	0.0063	1.67	94.14	70.79	4.17	456.83	23.78
10	100.0	82.607	0.533	-0.1886	0.0588	0.0009	0.0122	0.77	99.67	82.32	7.39	521.44	40.64
<b>AR-664 Anatectic granite biotite</b>													
1	2.8	74.623	0.162	0.0167	0.0195	0.0100	0.0034	2.74	95.98	71.63	2.04	461.60	11.59
2	23.2	73.705	0.100	0.0305	0.0007	-0.0020	0.0005	20.57	100.81	74.30	0.35	476.74	1.97
3	42.6	74.270	0.041	-0.0067	0.0049	-0.0007	0.0009	19.21	100.27	74.47	0.54	477.71	3.03
4	61.5	73.577	0.084	0.0019	0.0048	0.0008	0.0003	19.04	99.68	73.34	0.23	471.35	1.30
5	74.3	73.410	0.062	0.0058	0.0020	-0.0025	0.0010	12.68	101.02	74.16	0.64	475.97	3.60
6	85.2	73.691	0.098	-0.0301	0.0032	0.0012	0.0016	11.24	99.51	73.33	0.96	471.26	5.41
7	95.4	74.157	0.092	0.0581	0.0035	-0.0031	0.0009	9.94	101.24	75.08	0.58	481.15	3.24
8	97.3	73.385	0.774	-0.0296	0.0281	-0.0071	0.0049	2.05	102.88	75.50	3.35	483.48	18.83
9	99.6	78.937	0.837	-0.1303	0.0543	0.0023	0.0083	2.10	99.12	78.23	5.23	498.79	29.13
10	100.0	68.647	0.102	-0.1451	0.0947	0.0889	0.0156	0.44	61.33	42.09	9.31	285.31	58.38
<b>AR1133 Anatectic granite biotite</b>													
1	2.0	68.546	0.747	-0.0401	0.0538	0.0601	0.0021	1.85	73.83	50.60	1.62	337.89	9.85
2	14.1	76.158	0.025	-0.0042	0.0058	0.0021	0.0024	12.37	99.16	75.52	1.42	483.60	7.99
3	32.7	75.626	0.023	-0.0028	0.0024	-0.0009	0.0007	18.45	100.34	75.88	0.43	485.65	2.41
4	51.4	75.885	0.092	-0.0048	0.0024	-0.0025	0.0003	18.80	101.00	76.64	0.28	489.91	1.56
5	71.8	75.560	0.031	-0.0080	0.0008	-0.0011	0.0007	19.26	100.41	75.87	0.43	485.59	2.41
6	89.9	76.085	0.096	0.0030	0.0023	0.0001	0.0007	19.18	99.95	76.05	0.48	486.58	2.67

7	92.0	76.922	0.539	-0.0123	0.0164	0.0013	0.0057	2.09	99.49	76.53	3.57	489.26	20.02
8	94.5	77.429	0.277	0.0212	0.0221	-0.0021	0.0049	2.56	100.79	78.04	3.01	497.74	16.76
9	95.1	96.414	1.689	-0.0442	0.1504	-0.0416	0.0288	0.47	112.86	108.81	17.61	661.62	89.66
10	100.0	76.783	0.074	-0.0160	0.0135	0.0044	0.0026	4.72	98.28	75.46	1.56	483.27	8.78
<b>AR-1145 Diatexite biotite</b>													
1	3.8	76.081	0.461	0.0267	0.0152	0.0062	0.0045	3.76	97.58	74.24	2.84	476.40	15.99
2	19.7	74.885	0.098	0.0021	0.0036	0.0010	0.0008	16.04	99.61	74.59	0.49	478.38	2.78
3	41.7	74.068	0.056	0.0071	0.0018	-0.0005	0.0008	21.89	100.20	74.22	0.47	476.27	2.66
4	58.6	74.312	0.095	0.0352	0.0001	0.0008	0.0009	16.87	99.67	74.07	0.58	475.44	3.25
5	74.1	74.438	0.092	-0.0017	0.0032	-0.0002	0.0002	15.51	100.06	74.49	0.22	477.79	1.23
6	88.0	74.188	0.079	-0.0054	0.0063	0.0006	0.0003	13.97	99.75	74.00	0.26	475.07	1.45
7	94.9	74.099	0.070	-0.0330	0.0026	-0.0007	0.0024	6.67	100.29	74.31	1.46	476.81	8.26
8	97.2	78.537	0.256	0.0831	0.0015	0.0071	0.0031	2.62	97.31	76.43	1.91	488.71	10.68
9	99.1	75.991	0.233	-0.0308	0.0168	-0.0055	0.0056	1.92	102.16	77.63	3.37	495.42	18.82
10	100.0	103.780	3.899	-0.0479	0.2651	-0.0895	0.0691	0.22	125.76	130.51	42.35	768.85	203.22
<b>AR-1349 Metatexite biotite</b>													
1	2.6	75.148	0.048	0.0038	0.0193	0.0088	0.0044	2.41	96.52	72.53	2.61	466.73	14.82
2	18.7	73.699	0.043	-0.0035	0.0039	0.0003	0.0007	16.17	99.86	73.60	0.45	472.77	2.57
3	40.0	74.334	0.030	-0.0001	0.0033	0.0006	0.0003	21.43	99.77	74.16	0.18	475.97	1.04
4	57.9	73.908	0.031	0.0006	0.0036	0.0015	0.0008	17.85	99.41	73.47	0.48	472.07	2.73
5	74.3	73.914	0.012	-0.0028	0.0015	-0.0012	0.0005	16.36	100.50	74.28	0.29	476.65	1.64
6	86.4	74.232	0.069	-0.0049	0.0037	0.0003	0.0009	12.17	99.87	74.13	0.58	475.81	3.27
7	95.2	73.989	0.040	0.0236	0.0022	-0.0006	0.0006	9.04	100.24	74.17	0.39	475.98	2.18
8	97.6	73.159	0.180	-0.0378	0.0181	-0.0065	0.0038	2.19	102.65	75.09	2.30	481.21	12.97
9	100.0	78.291	0.116	-0.0526	0.0121	0.0012	0.0018	2.37	99.52	77.91	1.12	497.00	6.22
<b>AR-1368 Anatexitic granite biotite</b>													
1	3.1	68.182	0.009	-0.0421	0.0207	-0.0045	0.0055	3.11	101.96	69.52	3.30	449.57	18.87
2	22.3	71.413	0.029	-0.0048	0.0052	-0.0005	0.0011	19.35	100.20	71.56	0.69	461.21	3.92
3	44.1	72.785	0.110	-0.0071	0.0048	-0.0005	0.0006	21.88	100.21	72.94	0.41	469.04	2.35
4	58.8	72.960	0.067	-0.0014	0.0039	0.0001	0.0009	14.26	99.98	72.94	0.56	469.08	3.18
5	69.9	72.692	0.061	-0.0072	0.0089	-0.0033	0.0005	11.30	101.34	73.67	0.30	473.16	1.71
6	79.9	73.675	0.053	-0.0049	0.0073	0.0025	0.0007	9.95	99.00	72.94	0.40	469.06	2.29
7	88.5	72.897	0.099	0.0083	0.0088	0.0034	0.0007	9.67	98.63	71.90	0.45	463.14	2.53
8	95.2	73.578	0.007	-0.0601	0.0050	0.0050	0.0019	5.59	97.95	72.07	1.11	464.11	6.28
9	99.2	71.936	0.090	-0.0225	0.0173	0.0015	0.0032	4.26	99.39	71.49	1.92	460.85	10.90
10	100.0	72.199	0.996	-0.1665	0.0926	0.0304	0.0163	0.63	87.41	63.10	9.86	412.45	57.65

Koppers, A., 2012. ArArCALC v252: software for  $^{40}\text{Ar}/^{39}\text{Ar}$  geochronology, <http://www.earthref.org>.

Phillips, D. and Matchan, E.L., 2013a. Ultra-high precision  $^{40}\text{Ar}/^{39}\text{Ar}$  ages for Fish Canyon Tuff and Alder Creek Rhyolite sanidine: new dating standards required? *Geochimica et Cosmochimica Acta* 121, 229-239.

Steiger, R.H. and Jäger, E., 1977. Subcommittee on geochronology: convention on the use of decay constants in geo- and cosmochemistry. *Earth and Planetary Science Letters* 6, 359-362.